KURUSHINA, V., RAJENDRAN, V., PRATHURU, A., HOSSAIN, M., FAISAL, N., SOMAN, A., HORRI, B.A. and CAI, Q. 2023. Thermomechanical deformation analysis of a tubular solid oxide steam electrolysis cell. In Proceedings of the 34th Thermal and fluid analysis workshop 2023 (TFAWS 2023), 21-25 August 2023, Maryland, USA. Washington: NASA [online], article number TFAWS23-ID-7. Available from: https://tfaws.nasa.gov/tfaws23/proceedings/

Thermomechanical deformation analysis of a tubular solid oxide steam electrolysis cell.

KURUSHINA, V., RAJENDRAN, V., PRATHURU, A., HOSSAIN, M., FAISAL, N., SOMAN, A., HORRI, B.A. and CAI, Q.

2023

This file contains the paper and presentation slides combined into a single file for ease of use.

THERMOMECHANICAL DEFORMATION ANALYSIS OF A TUBULAR SOLID OXIDE STEAM ELECTROLYSIS CELL

Victoria Kurushina, Vinooth Rajendran, Anil Prathuru, Mamdud Hossain, Nadimul Faisal
School of Engineering, Robert Gordon University, Aberdeen, AB10 7GJ, UK

Ajith Soman, Bahman Amini Horri, Qiong Cai
University of Surrey, University Campus, Guildford, GU2 7XH, UK

ABSTRACT

Technologies behind electrolysis cells for hydrogen production are making progress in terms of portability, cost reduction, performance enhancement, prolonged operation, and integration in stacks and with existing power infrastructure. The solid oxide steam electrolysis technology is well suited for integration with existing sources of heat and electricity given its high temperature operation. This would lead to higher efficiencies compared to other electrolyser technologies. In this study, a tubular solid oxide steam electrolysis (SOSE) cell has been investigated for high-temperature conditions. The electrolysing reaction in the SOSE occurs across a series of layers, typical composition of which comprises multiple materials (metallics, ceramics). This means a significant mismatch in the thermomechanical behavior at a high temperature which leads to the damage build up over long operation times. To analyse the combined effect of boundary conditions, material composition, porosity variation, and pressure in the internal gas channel, a series of thermomechanical simulations using finite element analysis (FEA) technique has been performed for a tubular solid oxide cell design. The results indicate a significant tube elongation, which leads to stress accumulation near the fixed end connections. The maximum deformation is found to increase by about 1.4 times with the temperature elevation from 600 to 800 ^oC for non-porous materials. These effects can be substantially reduced if porous structures are used.

INTRODUCTION

Solid oxide steam electrolysis (SOSE) technology is developed on the intersection of applying solid materials, which exhibit specific conductivity properties in high-temperature conditions, and the conversion of both heat and electric energy into storable hydrogen fuel (Mougin 2015). Solid materials ensure the technology’s portability, transportation and handling convenience, while water, as an initial substance for hydrogen production, is exceptional for its’ ecological friendliness, availability, storability (Faisal, Prathuru et al. 2022). Although the SOSE can utilize a variety of feedstock materials. Recent studies related to the solid oxide electrolysis cells (SOECs) attempt to expand the range of feedstock options, advance the electrochemical efficiency, extend the lifetime of stacks and individual cells, simplify and scale fabrication, reduce costs, address challenges of integration with existing systems. Compatible systems, which can potentially benefit from the hydrogen production as a parallel process, span across several industries: nuclear energy (O'Brien, Stoots et al. 2010), renewable energy, including wind, tide, hydrothermal, solar energy sources (Karimi and Mehrpooya 2022, Wang, Wu et al. 2022, Kasaeian, Javidmehr et al. 2023), aviation (Bradley, Droney et al. 2015, Bingaman, Holly et al. 2022, Bradley 2022), space systems (Hwang, Rho et al. 2022), and may not be limited to it (Rostami, Manshadi et al. 2022). Despite challenges, the current state of technology already proves its suitability to support the development of sustainable energy projects on planet Earth, in space and on other planetary bodies.

Solid oxide electrolysis (SOE), proton exchange membrane (PEM) electrolysis and alkaline electrolysis (AE) are three prevalent methods for splitting water to produce hydrogen (Schmidt, Gambhir et al. 2017). The SOE operates in the range of 800-1000 ^{o}C leading to higher efficiencies due to the thermodynamics of water splitting at elevated temperatures. These extreme conditions affect the choice of materials and lead to durability challenges. Both PEM and alkaline electrolysis cells operate at ambient or near-ambient temperatures, up to 80 ^{o}C, a significantly lower temperature range. PEM electrolysis cells are considered to respond quickly to control signals and have excellent dynamic behaviour, coupled with a compact system design. PEM cells require expensive metal catalysts, and their durability depends on the acidic nature of the membrane. The alkaline electrolysis is currently a mature technology that involves cheaper catalyst materials and has an overall lower performance compared to PEM. Alkaline electrolysis cells are less suitable for the dynamic operation, due to a slower reaction kinetics and limitations on the mass transport in the alkaline electrolyte. The choice between these technologies depends on specific application requirements and related economic considerations. There is also currently a recognised demand for the development of SOE-based technologies and cell devices operating on an alternative basis for the temperature range from 300 ^{o}C to 600 ^{o}C, while retaining the efficiency of the hydrogen production on the level of alkaline and PEM electrolysis cells. Research in these directions will allow increasing the integrability of water electrolysis technologies and existing power infrastructures, where electricity and/or heat energy are underutilized.

Systems developed for spaceflight and challenging environments represent a very prospective niche for integration with electrolysis technologies, aiming at different operating temperatures, pressures, feedstock and resulting substances, including where conditions change rapidly. Excessive heating under direct sun rays can be accumulated as heat energy, in parallel to the use of solar arrays, and the heat can be transferred to a steam feedstock channel, directed to a stack of SOECs. This type of integration is plausible for many intermittently overheated systems, such as Earth-orbiting spacecrafts, spacecrafts on trajectories towards Venus, Mercury, Sun, where temperature differentials are greater, and permanent or temporary architectures designed for the lunar environment. In the case of water electrolysis, the output hydrogen and oxygen may be used as an extra fuel source. Additionally, SOEC represents a source of oxygen for the life support circuits in potential habitat infrastructures on Moon and Mars (Harris, Kessler et al. 2022, Choate, Harris et al. 2023, Goodliff, Merancy et al. 2023), accounting for the potential water availability in the Martian soil, and the sizes of SOEC stacks are flexible enough and could be adapted to the system’s necessity.

The solid oxide technology has already been used for a number of missions in space, mainly integrated in the systems of landers, rovers and probes, supporting exploratory activities at remote cites (Ryan, Araghi et al. 2013, Meyen, Hecht et al. 2016, Meyen 2017, Hartvigsen, Elangovan et al. 2018, Jakupca 2021, Green, Elangovan et al. 2022). Here, SOFC is used to generate electricity which can further be used for various purposes. Space exploration purposes are often linked to large variations in external conditions, so that the specific demand of the industry can be predicted to focus on the reversible SOFC/SOEC, suitable for an intermittent operation in either mode. One of well documented challenges for the use of solid oxide technology in space environments is related to isolation of the high-temperature fluids, including feedstocks, stacks of cells, storage volumes, which requires a rigor material selection and mechanical stability (Steinetz, Bansal et al. 2004, Bansal and Choi 2007, Bansal, Hurst et al. 2007).

Recent developments in the field of metamaterials, allowing a structured composition of materials at various length scales, are another dimension of progress for the improvement of solid oxide technology (Faisal, Sellami et al. 2021), including for space exploration purposes. Application of metasurfaces, layers of extreme aspect ratios, in combination with the general cell layout, material types and fabrication routes are an area of ongoing innovation, which is only possible on the intersection of disciplines. Previous works have established that one of the ways to unlock the electrolysis or fuel cell efficiency is in increasing the surface area of electrochemically active zones, while the overall cell volume and mass remain relatively similar, which is important for a payload. Metamaterials can play a great role in creating new and complex surfaces for both SOFCs and SOECs, however, the optimal recipes for the design and fabrication will be substantially different between these two.

Handling complex designs and carrying out comprehensive optimizations at the cell and stack levels can be approached by several methods and with commercially available software packages. Computational fluid dynamics (CFD), structural and thermal process analysis on their own and in multiphysics set-ups allow approaching a broad range of challenges (Li, Zhang et al. 2021). Several challenges, such as stack lifetime, material degradation and process efficiency, are often prioritized in design development as critical for the technology overall. Computational analyses for this problem are mainly based on the finite element and finite volume methods and allow both steady-state and transient simulations (Mottaghizadeh, Fardadi et al. 2021). Thermomechanical simulations here represent a specific interest, to account for the working and extreme conditions and foresee any issues with the mechanical stability of the cell. Delamination process is particularly important at the micro- and nanoscale, as the cell efficiency is closely correlated to adhesion of thin electrolyte, cathode and anode layers. Here, large deformations identified with the thermal analysis can substantially reduce the cell efficiency, hence, this is important to recognize design areas subject to deformation.

The current study aims to estimate and understand the thermomechanical deformation of the multilayer SOSE electrode subject to high temperatures, using the finite element method (FEA) based numerical calculations, to ensure mechanical stability. Analysis attempts to simulate, first, the range of intended high-temperature operating conditions, and second, to obtain estimates for some extreme combination of parameters, with a safety margin to the working conditions.

These assessments for the specific tubular design of interest will become a basis for further design iterations, involving fluid dynamics and electrochemical efficiency estimates.

The present paper is organized in four sections, where introduction provides an overall background for the role of SOEC in present and the significance of thermal analysis in the cell development. Model section is designed to outline the tubular cell model and the work done towards the verification of a multi-layered structure model. Results part has four subsections, where effects due to material properties and high temperature conditions are considered. Conclusions present a summary of the thermomechanical SOEC analysis.

MODEL

The system considered in this paper is a single SOE tubular cell operating in the temperature range of 600-1000 ^{o}C. The SOE process is an electrochemical summary of the ion transfer, reduction and oxidation reactions, occurring at the cathode and anode layers, as shown in Fig. 1(a). The tubular cell design in this study is metal-supported, as illustrated in Fig. 1(b), which generally allows a better mechanical stability and suitable energy losses during the particle transfer, compared to alternative cathode-, electrolyte- and anode-supported designs. A full breakdown of six layers considered in the thermomechanical analysis is provided in Table 1.

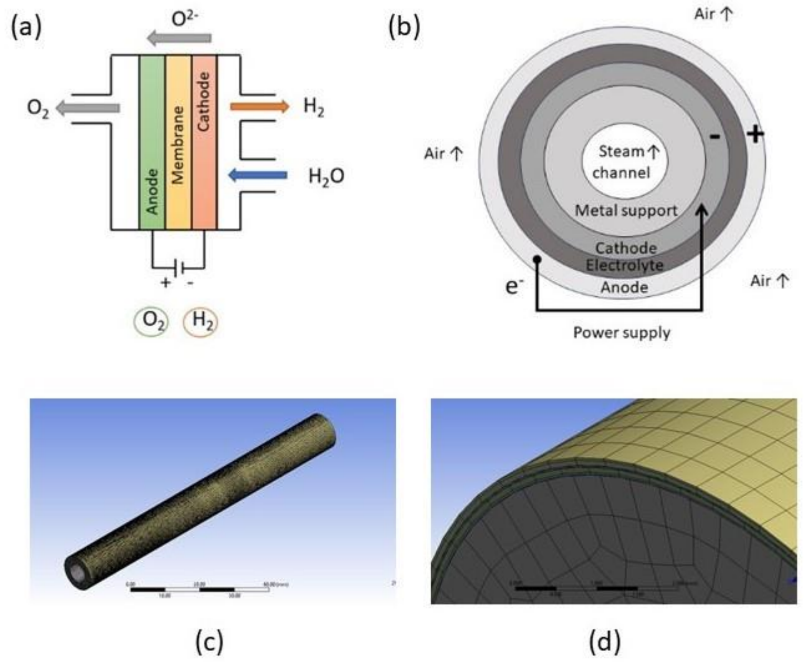

Figure 1. SOEC schematic: (a) basic electrochemistry of the solid oxide electrolysis process; (b) general view on the tubular SOEC with a thick metal support; (c) cell geometry and mesh sample to the simulation scale and (d) enlarged.

Table 1. Summary table of layers and materials

Layer	Functionality	Thickness (per design), mm	Material	Porosity (per design), %
1	**Substrate (metal substrate)**	**2.150**	**Titanium alloy**	**30**
2	**Interconnect / Current collector**	**0.035**	**Silver**	**0**
3	**Cathode**	**0.070**	**Nickel oxide and GDC**	**30**
4	**Electrolyte**	**0.022**	**GDC and YSZ**	**0**
5	**Anode**	**0.070**	**GDC and LSCF**	**30**
6	**Interconnect / Current collector**	**0.035**	**Silver**	**30**

The metal substrate supporting tube, the thickest layer in Fig. 1(c), of 100 mm length and 6 mm internal diameter is porous to ensure a sufficient conductivity of species towards electrochemically active cell zones. The relative proportion of thickness for the active layers, responsible for the electrolysis, is demonstrated in Fig. 1(d). Here, the dense electrolyte layer is one of the most critical areas, where the low thickness allows smaller ohmic losses. This makes the thermomechanical analysis of the electrolyte layer specifically critical, because any fractures in the 0.022 mm thick structure can directly compromise the cell performance.

Properties of layers, summarized in Table 1, are incorporated in the present thermomechanical analysis in a simplified manner in the way to account for the worst-case scenario of expansion of a non-porous metal and ceramics, constrained at both ends, and expansion of the cell with an ideal designated porosity. Other simplifications include the substrate material, assumed to have properties of the alloy Ti-4V-Al, due to the high temperature data availability, and the outer interconnect layer in simulations is assumed to be a uniform porous layer, rather than an equally spaced wrapping wire.

Materials, listed in Table 1, from the intended tubular cell design include nickel oxide, gadolinia-doped ceria (GDC), yttria-stabilized zirconia (YSZ) and lanthanum strontium cobalt ferrite (LSCF), that are quite specific to the application area. For this reason, their properties for simulations are taken from the literature, as summarized in Table 2. These data are processed in order to account for the mass or volume fraction in the designed layers, mentioned in Table 1, and these materials are manually included in the material library, as specified in Table 3 per layer.

Table 2. Material properties

Material	**Density, kg/m^3**	**Melting temperature, °C**	**Young's modulus, GPa**	**Poisson ratio**	**Thermal expansion coefficient, µm/m·°C**	**Tensile yield strength, MPa**	**Ultimate yield strength, MPa**
Titanium alloy	**4405**	**1370**	**107**	**0.32**	**8.9**	**850**	**1098**
Silver	**10500**	**961**	**83**	**0.37**	**19**	**54**	**140**
Nickel oxide	**4670**	**1605**	**160**	**0.26**	**12.5**	**440**	**646**
GDC	**7200**	**2600**	**120**	**0.26**	**11.5**	**1.95**	**200**
YSZ	**5900**	**2700**	**210**	**0.28**	**10.5**	**750**	**1200**
LSCF	**6000**	**920**	**170**	**0.30**	**14.5**	**94**	**160**

Table 3. Properties of mixed layers incorporated in the simulation

Property	**Units**	**Cathode**	**Electrolyte**	**Anode**
Density	kg/m^3	5682	7082	6600
Melting point	°C	2003	2609	1760
Young's modulus	GPa	144	128	145
Poisson's ratio		0.26	0.26	0.28
Thermal expansion coefficient	µm/m·°C	12.1	11.4	13
Tensile yield strength	MPa	265	24.5	48
Ultimate yield strength	MPa	467	223	180

The Static Structural module of the ANSYS software generally solves the force balance with the finite element methodology, which could be presented as a matrix equation, accounting for the acting forces, stiffness matrix and displacement vector. This force balance in a steady-state at a high temperature is solved for every element with the Newton-Raphson methodology.

The numerical model for the thermomechanical analysis in this study uses standard solid body elements with three degrees-of-freedom (3DOFs) for the relatively thick substrate tube and uses shell elements with six degrees-of-freedom (6DOFs) for the five functional layers. Shell elements in ANSYS do not account for the compression through the thickness, their formulation includes a membrane and bending behavior. The combined use of the shell and standard solid body elements in the model leads to the definition of contact regions as bonded, with the build-in Model Predictive Control (MPC) formulation.

Mesh independence test for further thermomechanical studies is performed for the 0% porosity level in all layers and fixed-fixed boundary conditions, - conditions allowing a demonstration of the worst case scenario thermal expansion of the tubular cell at all levels. The internal steam fluid channel is a source of the pressure load, acting on the internal surface of the substrate tube, with the value of 1 MPa. This is due to the laboratory experiments in the current Project planned for the pressure range of 0.5 to 1 MPa in fluid channels. The mesh independence test is conducted for the medium temperature of 800 ^{o}C in the target high temperature range, and the results are presented in Table 4. Based on these data, the grid with 90 762 elements in total for the six layers model has indicated a sufficient accuracy of the maximum total deformation estimates in the outer interconnect layer and in the inner substrate layer. This resolution is used to obtain results of the thermomechanical analysis, presented in the following section.

Table 4. Mesh independence test

#	Number of cells	Maximum total deformation of the outer silver interconnect, mm	Maximum total deformation of the titanium substrate, mm	Grid and model features' summary
1	22 537	0.10441	0.079562	Standard elements for substrate, shell elements for five functional layers, full tube of 100 mm, bonded contacts
2	37 862	0.11159	0.078981	
3	50 962	0.11234	0.078593	
4	76 192	0.11036	0.078641	
5	**90 762**	**0.088686**	**0.078468**	
6	118 342	0.094807	0.078269	
7	129 009	0.087868	0.079190	
8	141 911	0.089302	0.078229	

RESULTS

Thermomechanical results are organized in four subsections: analysis of a stress condition along the length of the 100 mm long cell; considering the effect of boundary conditions; analysis of the temperature impact, and study of the effect of porosity. These results identify the areas where the delamination, cracking and related lack of electrochemical performance can be expected, so that the tubular SOEC can be designed to avoid these conditions, including the arrangement of laboratory tests for a single cell at high temperature conditions and the stack design, where appropriate sealing should be balanced with the cell expansion.

In order to account for the effects of porosity, properties of layers' materials are modified, as given in Table 5, in a simplified manner, so that the 30% design porosity in layers 1, 3, 5 and 6 reduces these characteristics by 30%. Results for normal stresses are presented below for the selected cross-sections at 25 mm, 50 mm and 75 mm distance from one of the fixed ends of the cell, and the cross-sections are schematically shown in Fig. 2(a). Stresses are identified with respect to the cylindrical coordinate system shown in Fig. 2(b), placed in the same origin with the global Cartesian coordinate system, so that the radial X direction coincides with the Cartesian X axis. Locations of the displayed stresses, through the thickness of the structure, are schematically shown in the cross-section in Fig. 2(c) and marked as A-1 – A-2, B-1 – B-2, C-1 – C-2 and D-1 – D-2. Here, the 0^{o} line is consistent with the positive direction of X axis, pointing from the centre of the cross-section outwards. The line at 90^{o} respectively corresponds to the positive direction of the Y axis in Cartesian coordinates.

Table 5. Properties of layers with design porosity of 30% at 20^{o}C

Property	Units	Titanium alloy	Cathode	Anode	Silver interconnect
Density	kg/m^3	3084	3977	4620	7350
Young's modulus	GPa	74.9	101	102	58.1
Thermal expansion coefficient	μm/m·°C	6.23	8.5	9.1	13.3
Tensile yield strength	MPa	595	186	34	38
Ultimate yield strength	MPa	769	327	126	46

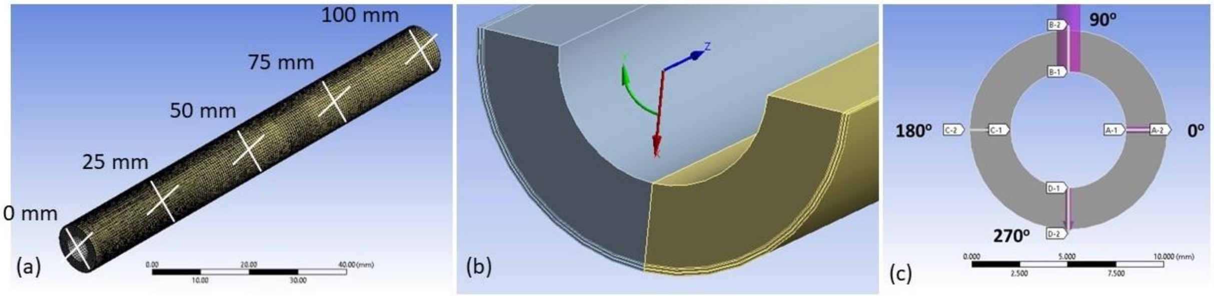

Figure 2. Geometrical locations of stresses: (a) locations of cross-sections along the length of the tubular cell; (b) cylindrical coordinate system placed in the origin of the global cartesian coordinate system in the centre of the cross-section at 0 mm mark; (c) four stress locations around the cross-section, where 0^{o} corresponds to the direction of X axis in both coordinate systems.

Stress analysis of the non-porous structure at 800^{o}C

Temperature elevation to 800^{o}C for the SOEC leads to the deformation build up near the fixed ends and with bending effects, as seen in the contour plots in Figs 3 and 4 for each of six layers. Here, the electrolyte layer (Layer 4) has the lowest coefficient of the thermal expansion, as mentioned in Table 3, so that the deformation of layers under the dense electrolyte is relatively limited by its expansion. Resulting deformation values across the tube for Layers 1-2 and Layers 3-4 are, hence, relatively similar, while Layers 5 and 6 demonstrate different types of expansion, driven by both radial and Hoop stresses. Comparison of Figs 3 and 4 demonstrate uneven, asymmetric deformation around the tube circumference, with the maximum observed value of about 0.0887 mm near one of the fixed ends.

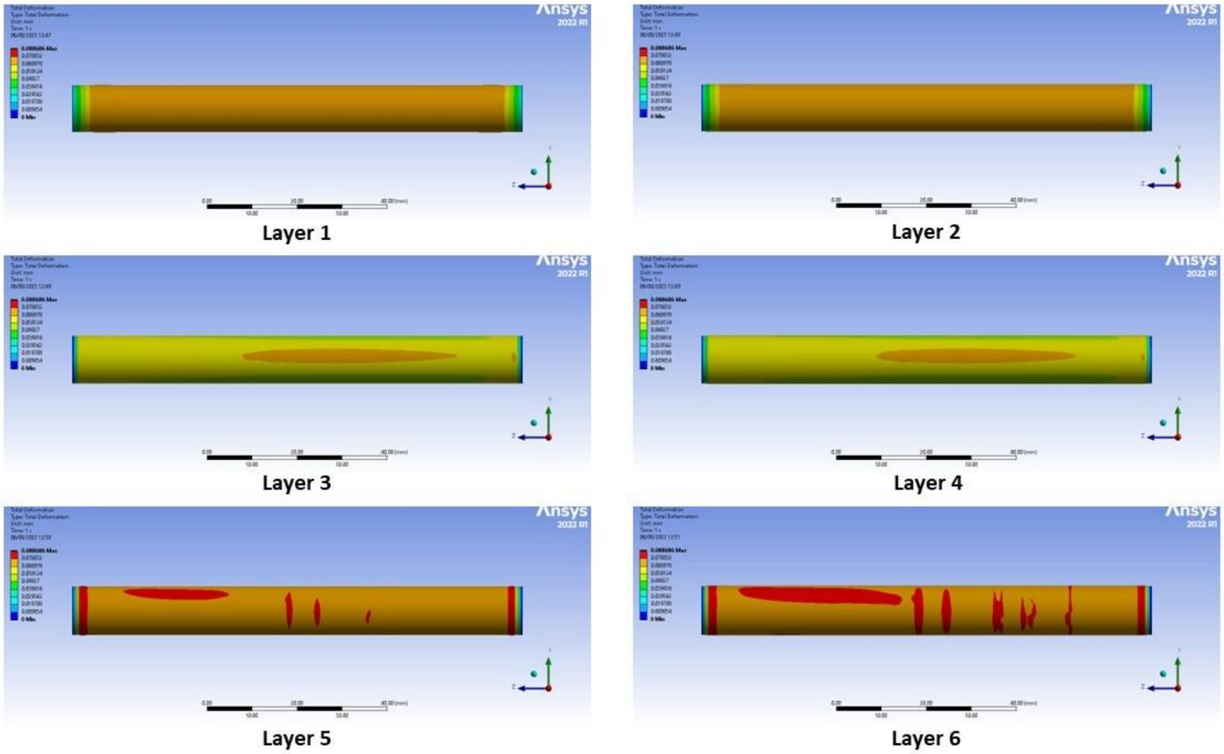

Layer 1 Layer 2

Layer 3 Layer 4

Layer 5 Layer 6

Figure 3. Contours of the total deformation in terms of six functional layers, as seen from the positive direction of the X axis, for the fixed-fixed boundary conditions, the temperature of 800^{o}C and non-porous structure.

A detailed view on the normal stresses in these conditions is given in Fig. 5. This figure demonstrates a limited variation of stress values for the selected locations at 0^o to 270^o in the cross-section, however, at least, one direction (here, at 0^o) demonstrates a higher variation of the radial and Hoop stress in the substrate. In this direction, larger stresses are experienced in the cross-sections of 25 and 75 mm from the selected fixed end of 0 mm, compared to the middle cross-section.

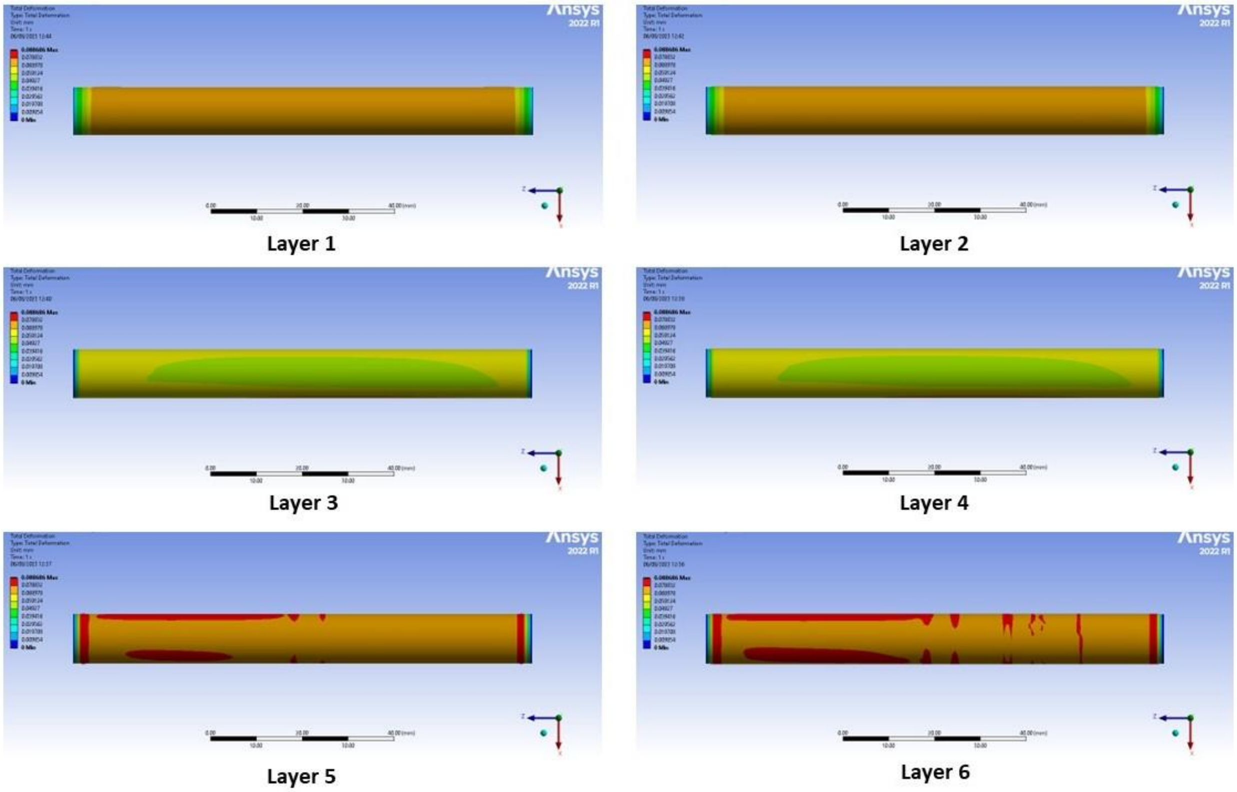
Layer 1
Layer 2
Layer 3
Layer 4
Layer 5
Layer 6

Figure 4. Contours of the total deformation in terms of six functional layers, as seen from the positive direction of the Y axis, for the fixed-fixed boundary conditions, the temperature of 800^{o}C and non-porous structure.

Effect of the cell constraints

Analysis of the fixed-free boundary conditions for the “worst case” non-porous structure indicates the maximum total deformation of 1.129 mm expected at 800 ^{o}C, as shown in Fig. 6, an order of magnitude larger than any deformation seen in the fixed-fixed state. Here, functional layers expand more significantly than the metal substrate, though the lower CTE of the electrolyte layer has some limiting effect on the resulting deformation. Thermal expansion in the direction of the free end reduces magnitude of the longitudinal stresses in the substrate and functional layers, as illustrated in Fig. 7. These results indicate an increase in the radial stresses for all sampling locations and a relatively low impact on Hoop stresses.

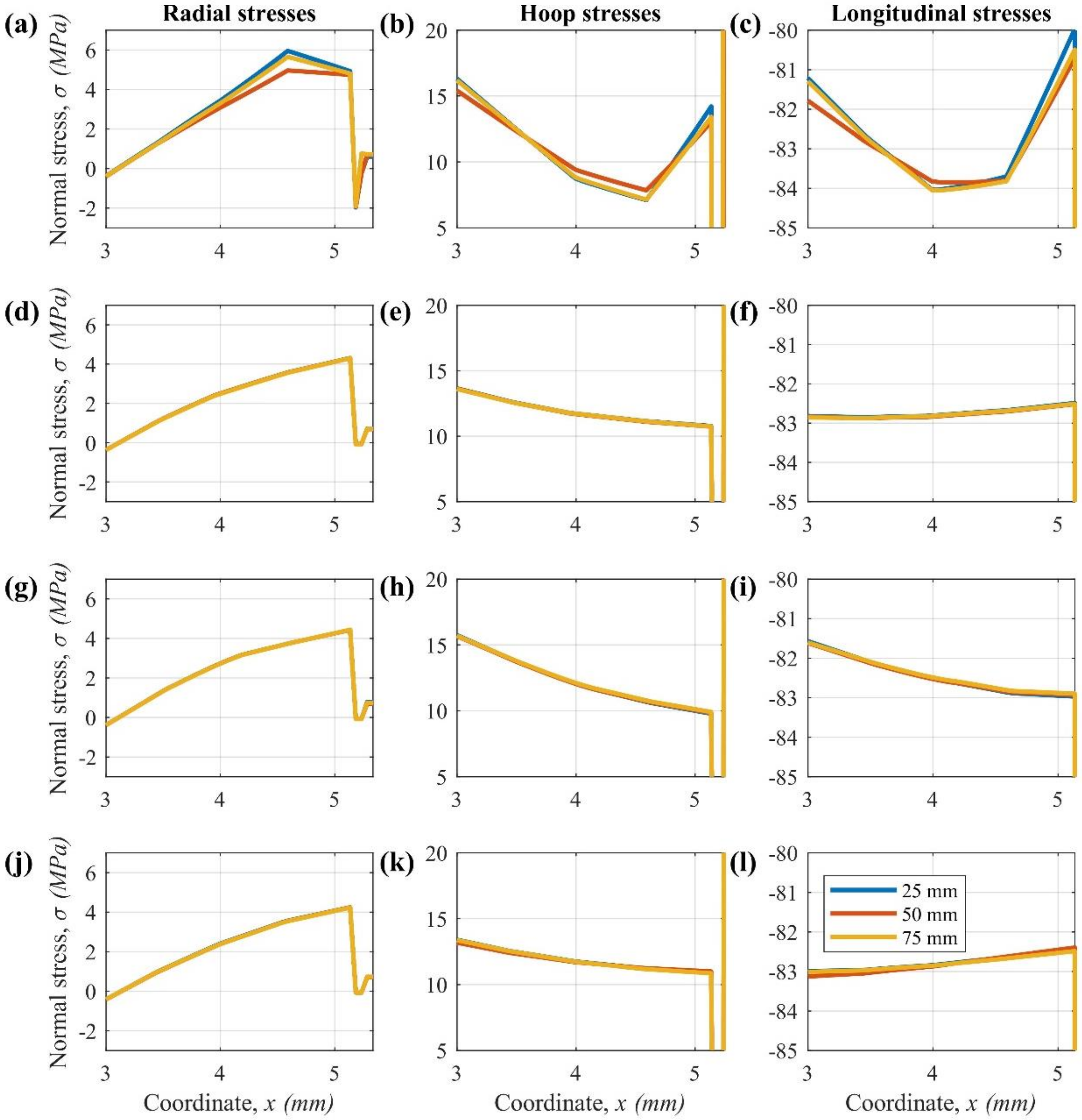

Figure 5. Variation of the normal stresses for three cross-sections along the wall coordinate with fixed-fixed boundary conditions: (a)-(c) at 0°; (d)-(f) at 90°; (g)-(i) at 180°; (j)-(l) at 270°. Here, the positive X axis direction is considered to be 0°. The view is enlarged.

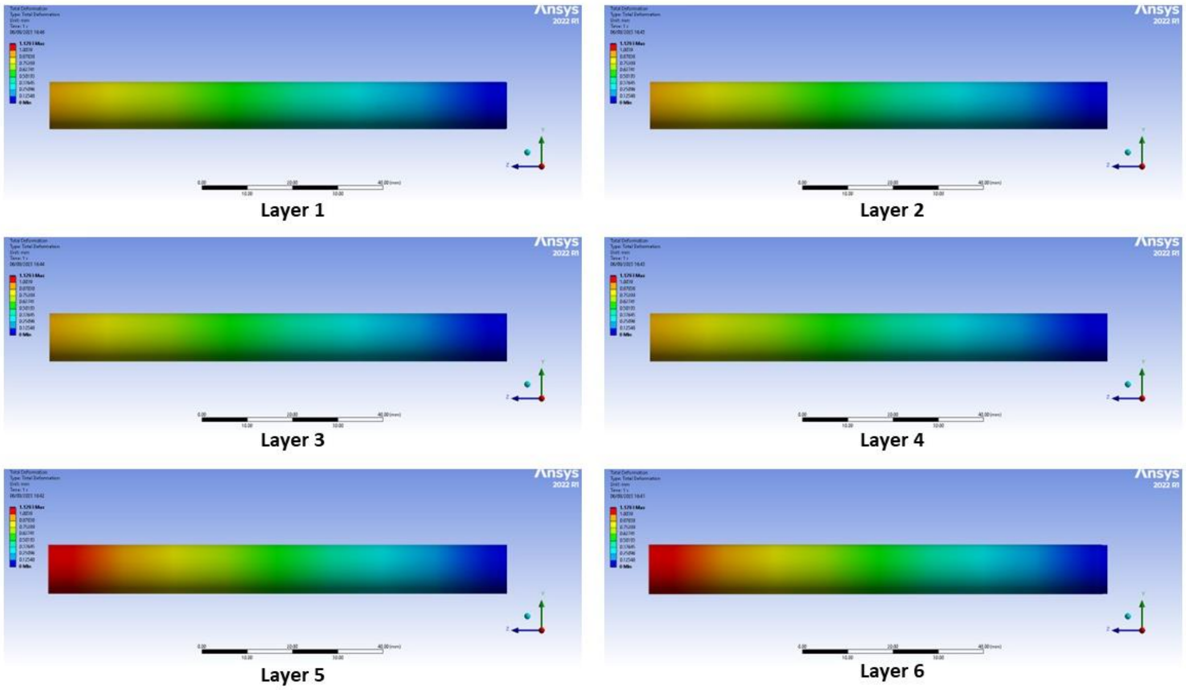

Layer 1

Layer 2

Layer 3

Layer 4

Layer 5

Layer 6

Figure 6. Contours of the total deformation in terms of six functional layers, for the fixed-free boundary conditions, temperature of 800°C and non-porous structure.

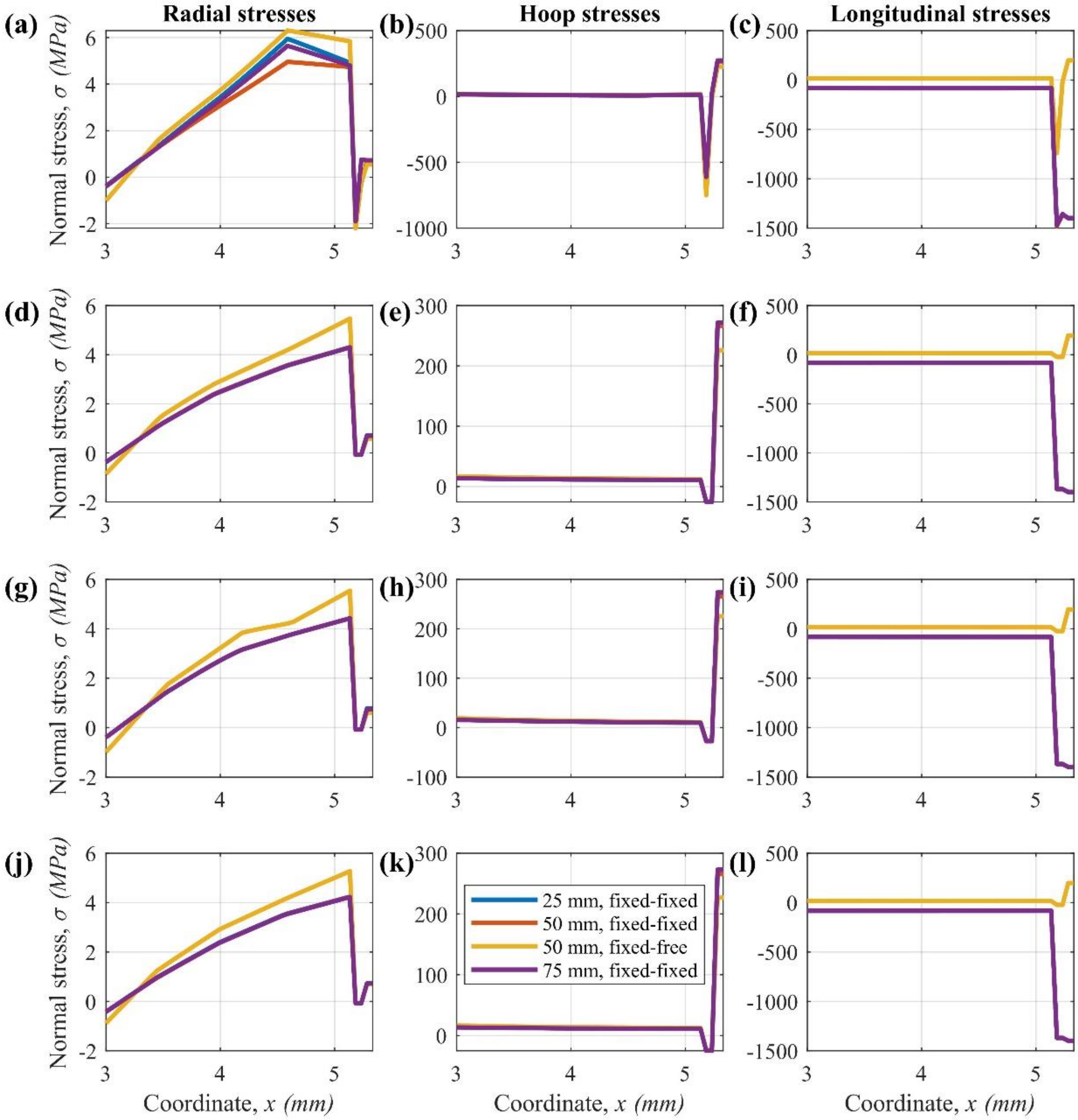

Figure 7. Comparison of the fixed-fixed and fixed-free boundary conditions in terms of the variation of normal stresses for three cross-sections along the wall coordinate: (a)-(c) at 0°; (d)-(f) at 90°; (g)-(i) at 180°; (j)-(l) at 270°. Here, the positive X axis direction is considered to be 0°. This is the full view (no scaling).

High temperature effects in the SOEC model

Effect of the increasing temperature for the SOEC model with non-porous materials is shown in Fig. 8(a) in terms of the maximum total deformation. Here, the heating from 600 ^{o}C to 800 ^{o}C appears to be very important in building up the deformed condition, as the maximum deformation increases about 1.4 times, with the progression of this trend to the upper bound of the considered temperature range. Figure 9 illustrates the most critical deformation state in the current thermomechanical simulations at 1000 ^{o}C for the 0% porosity. The maximum total deformation in this case is 0.111 mm, achieved near one of the fixed ends of the cell model. As shown in this figure, the deformed condition is developed to form multiple areas of the potential crack and delamination occurrence near the fixed boundaries and in the longitudinal direction. The areas near boundaries demonstrate a relatively larger overall deformation, starting at the level of the supporting metal substrate. The outer interconnect layer additionally shows a variety of the deformed zones of a circular and elongated configuration on the sides of the cell.

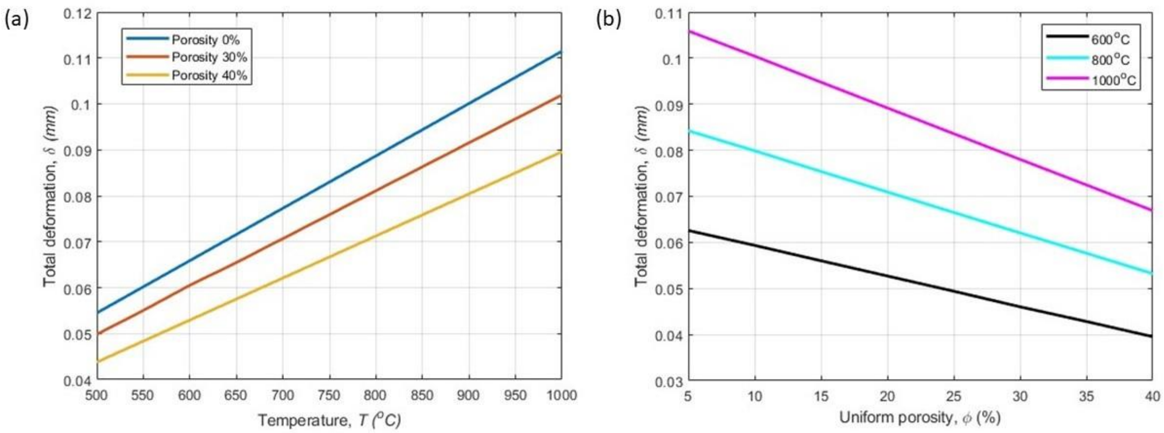

Figure 8. Maximum total deformation of the fixed-fixed porous and non-porous SOEC models in comparison: (a) with the porous layers 1, 3, 5, 6; (b) with porosity in all six layers.

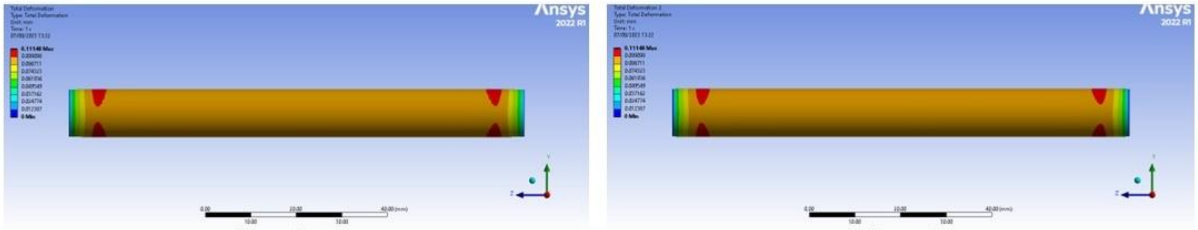

Layer 1 Layer 2

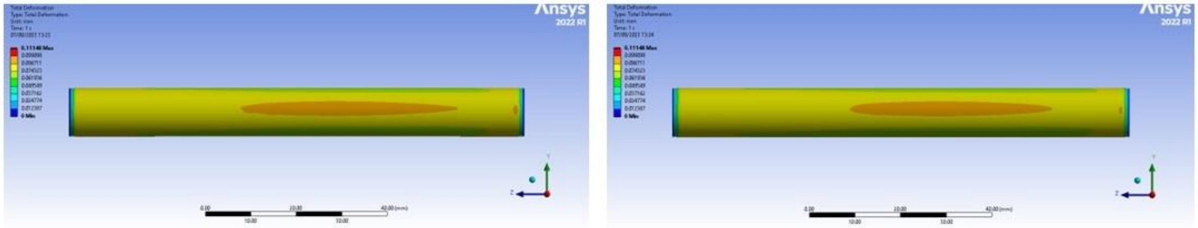

Layer 3 Layer 4

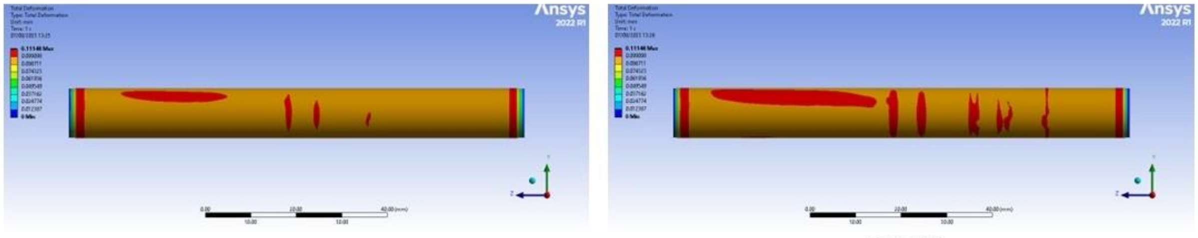

Laver 5 Layer 6

Figure 9. Contours of the total deformation of the non-porous SOEC model at 1000 ^oC with fixed-fixed boundaries from X axis.

Effect of porosity on the thermal expansion of the SOEC structure

Effect of porosity on the deformation of the tubular cell can be estimated based on results in Figs 8, 10-14. Starting with the lower bound of the shown temperature range, 500 ^oC, implementation of the 30% porous layers 1, 3, 5, 6, according to the proposed design in Table 1, leads to a significant reduction in any observed thermal deformation, and this reduction can be quantified at the level of 10%. Figure 8(a) also demonstrates a significant difference between the level of expansion at the 30% and 40% porosity levels, therefore, a change to the 40% porous layers (from 30%) leads to an additional 10% reduction in the maximum total deformation. According to simulations, this pattern characterizes all the considered temperature range from 500 ^oC to 1000 ^oC.

At the same time, the variation of porosity, which is identical in all layers of the SOEC model in Fig. 8(b), has a nearly linear effect on the increase of the total deformation of the outer layer. Maximum total deformation of an SOEC at 1000 ^oC is 0.102 mm at the 30% porosity in layers 1, 3, 5, 6 and 0.078 mm at the 30% porosity in all six layers, or 1.3 times difference between the designed and uniform porosity levels. Figure 8 also shows that the maximum total deformation at 1000 ^oC at 40% porosity in layers 1, 3, 5, 6 is 0.090 mm vs. 0.067 mm at 40% uniform porosity and the same temperature, or 1.34 times difference. Despite differences in values of the total deformation among the heated non-porous, uniformly porous and partially porous SOEC models, the maximum total deformation is observed for all of them in one of the circular deformed zones near one of the fixed ends, away from the middle cross-section.

Figure 10 illustrates how the radial, Hoop and longitudinal stresses evolve along the radial coordinate with the elevation of temperature and changes in porosity for a single sample direction of 0°. Radial stresses in Fig. 10(a) vary significantly in the substrate when temperature is at the lower bound of the operating temperature range (600 °C), for the non-porous tube model. A more deformed structure at the top of the temperature range at 1000 °C reduces the variation of radial stresses within the substrate. At the same time, Hoop and longitudinal stresses grow in the magnitude for all the functional layers, as illustrated in Figs 10(b) and 10(c). The radial stress grows more smoothly within the substrate, when the structure is partially porous, as appears in Fig. 10(d), while changes in the functional layers are much less significant. The heating also leads to a significant variation of the longitudinal stress in the substrate for both non-porous structure in Fig. 10(c) and partially porous structure in Fig. 10(f). The Hoop stress appears to be more affected by the porosity than the heating, especially, for the functional layers.

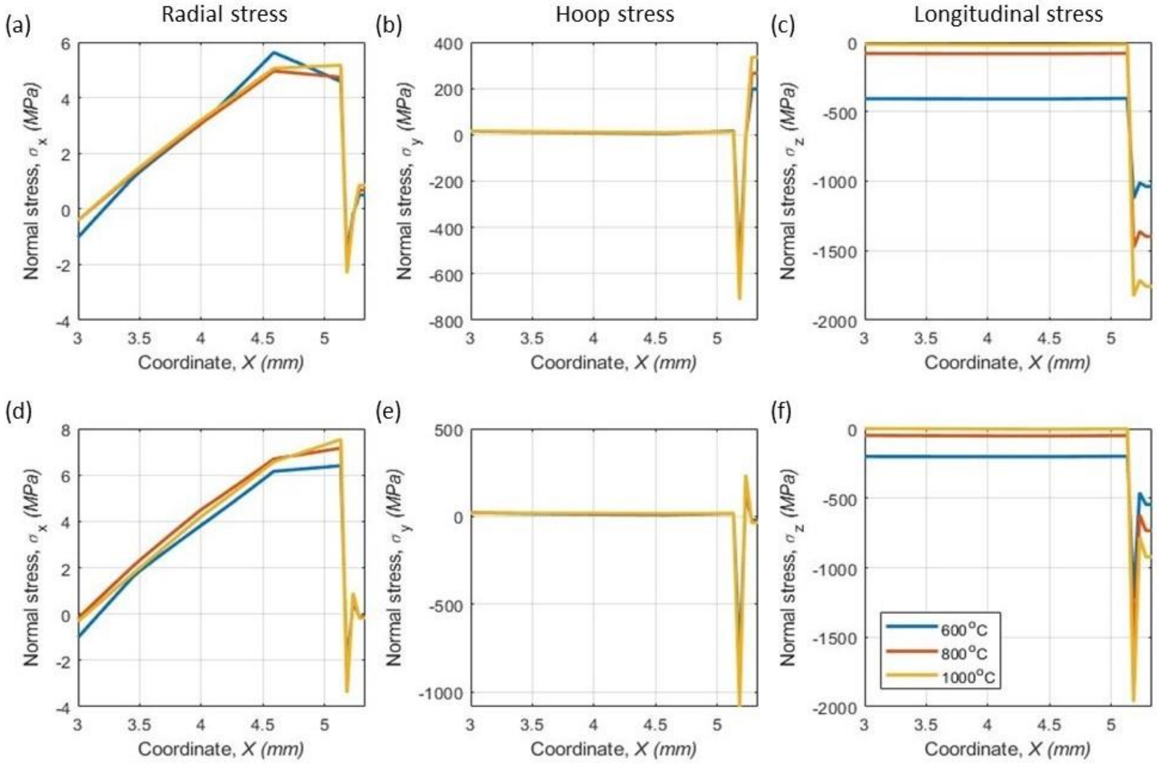

Figure 10. Effect of high temperature on normal stresses at for 0°: (a)-(c) porosity 0%; (d)-(f) porosity 30% in layers 1, 3, 5, 6.

Figures 11-12 provide a more detailed view on the resulting deformation of a partially porous cell, as per design. At the level of the substrate (Layer 1) and the inner silver interconnect layer (Layer 2), a higher deformation is visibly concentrated around the tube bounds for both 30% and 40% porosities, while changes to the outer interconnect layer are dominated by the deformation of an elongated configuration on the sides of the SOEC. Compared to Figs 3, 4, 9, these contour plots indicate a lack of previously significant multiple circular shaped zones of deformation in the outer silver interconnect layer in the middle sections of the cell. In contrast, Fig. 13 indicates that deformation zones at 1000 ^{o}C and uniform porosity of 40% are more consistent with the expansion of the non-porous cell, except for the lower overall total deformation with the maximum of 0.067 mm (vs. 0.111 mm for the non-porous structure).

Effect of porosity on normal stresses is presented in Fig. 14, where the nonlinear trend in the maximum total deformation decreasing with increase in porosity of layers 1, 3, 5, 6, as in Fig. 8(a), correlates with nonlinear growth of all stresses in the substrate in Figs 14(a)-14(c). A mixed effect is observed in the Hoop stress for the functional layers, as indicated in Fig. 14(b). At the same time, effects of the uniform porosity in Figs 14(d)-14(f) are relatively predictable, and the porosity growth leads to the reduction in all magnitudes of normal stresses, either in the substrate or in the functional layers.

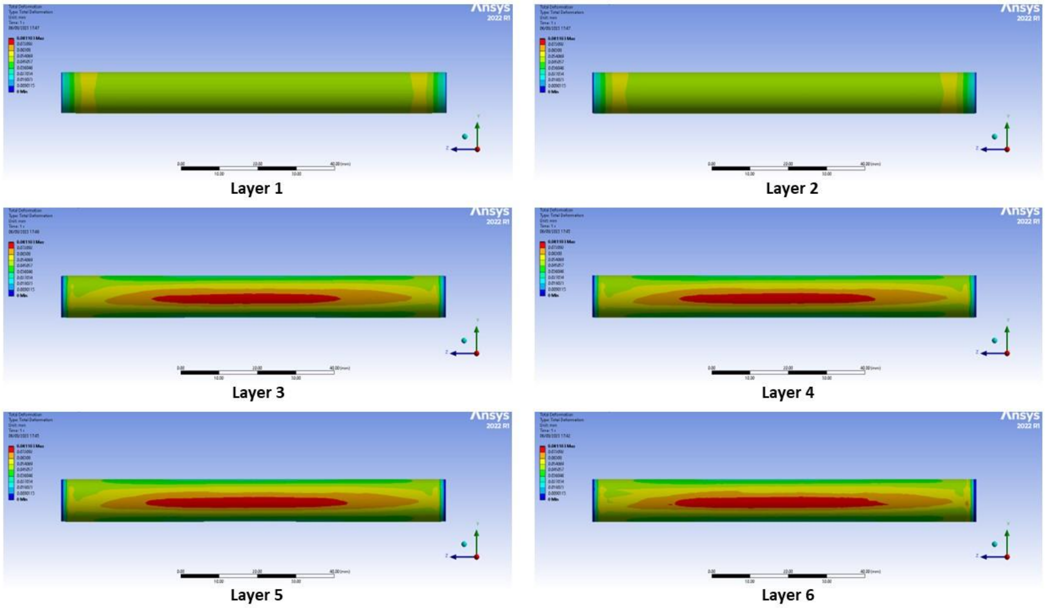

Layer 1

Layer 2

Layer 3

Layer 4

Layer 5

Layer 6

Figure 11. Contours of the total deformation of the 30% porous (in layers 1, 3, 5, 6) SOEC model at 800 ^{o}C with fixed-fixed boundaries.

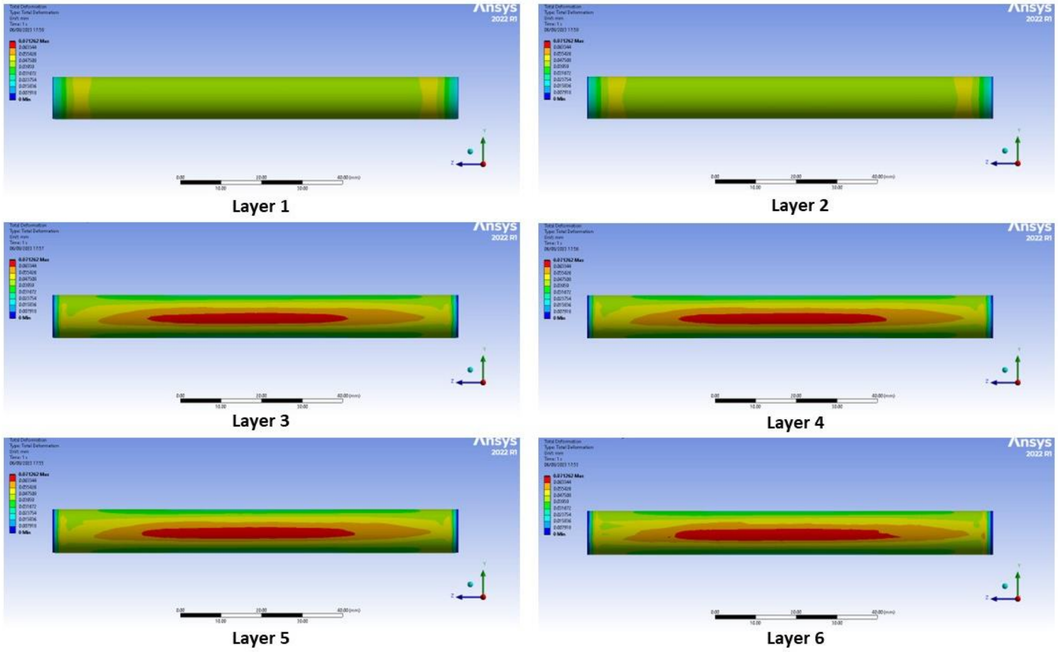

Figure 12. Contours of the total deformation of the 40% porous (in layers 1, 3, 5, 6) SOEC model at 800 ^{o}C with fixed-fixed boundaries.

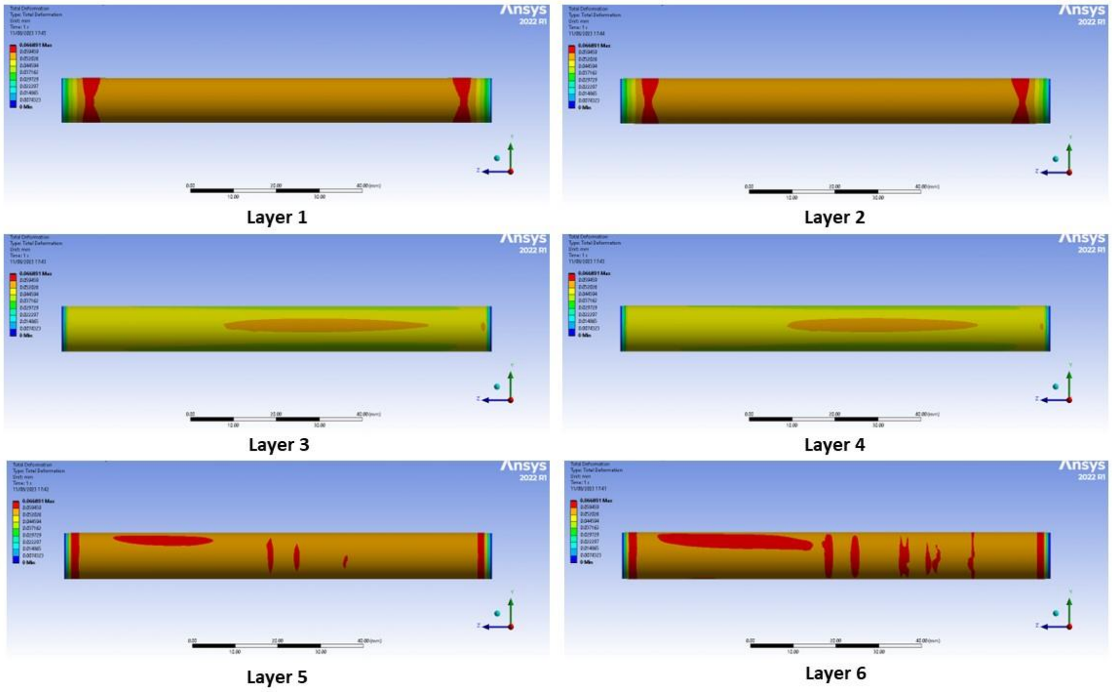

Figure 13. Contours of the total deformation of the SOEC model at 1000 ^{o}C with fixed-fixed boundaries at 40% porosity in six layers.

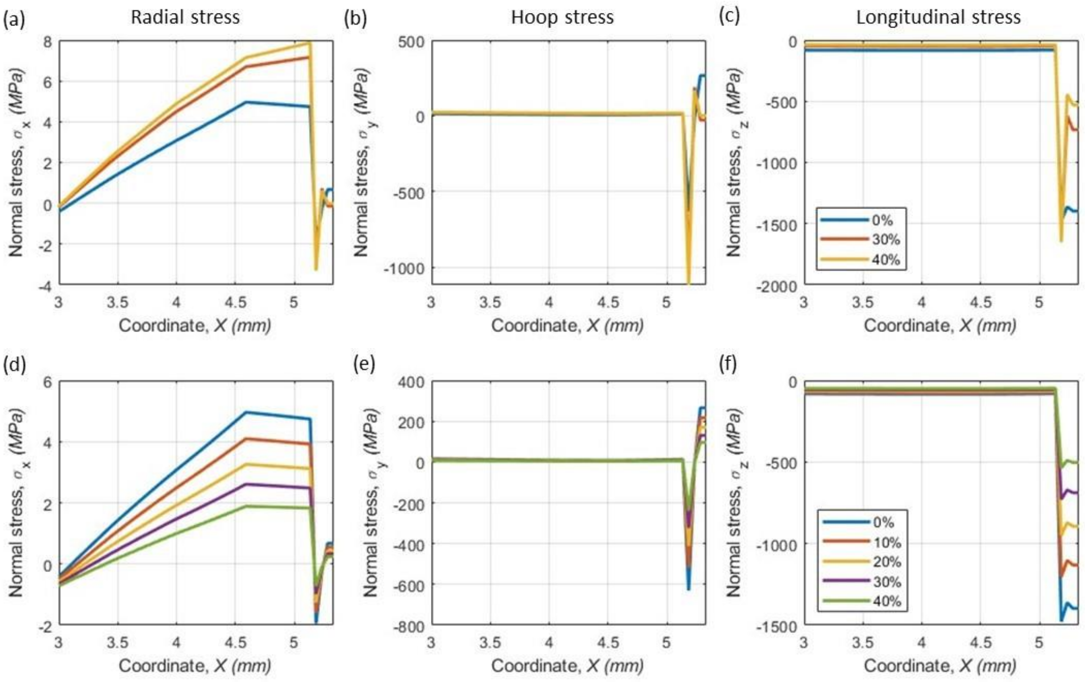

Figure 14. Effect of porosity on normal stresses at 0°: (a)-(c) effect of porosity in layers 1, 3, 5 and 6; (d)-(f) effect of porosity in six layers.

CONCLUSIONS

A series of thermomechanical simulations with the high temperature deformation of the tubular SOEC model is performed in this work. Effect of the increasing temperature from 600 °C to 800 °C is estimated to be as high as about 1.4 times in terms of the maximum total deformation of the non-porous structure. The thermal expansion effects become specifically pronounced above 600 °C, where the deformation of layers 1 to 3 is partially limited by the electrolyte layer, which has the lowest coefficient of the thermal expansion among the functional layers. At 1000 °C, at least, one of the considered materials is above it's melting temperature, and the deformation at this temperature is the most significant – at the level of 0.111 mm near one of the fixed ends.

The porosity of 30%, apart from increasing the electrochemically active area, as proposed in the initial design for layers 1, 3, 5, 6, allows reducing the deformation at a high temperature substantially. In simulations, a further increase to the 40% porosity in the selected layers is found to allow even a more efficient reduction in the structural expansion, than raising porosity from 0% to 30%. The porosity level in the selected layers reduces a number of circular deformed zones along the length of the cell, leaving circular deformations near the fixed ends, while elongated deformations dominate at the middle of the cell. This is where the cracks and delamination are most expected for the main design case. A more uniform porosity in all considered cell layers is found to lead to a more predictable reduction in normal stresses for both metal substrate and the functional layers, than when using layers with a different porosity level.

These results of thermomechanical simulations contribute to further improvements in the overall design of the tubular SOEC and foreseeing potential effects in the planned high temperature laboratory tests.

ACKNOWLEDGEMENTS

The authors acknowledge high temperature steam electrolysis related funding by the UKRI EPSRC via Grants No. EP/W033178/1 (METASIS). Authors (NF, AP, MH) acknowledges thermochemical electrolysis related funding by UK National Nuclear Laboratory (NNL) via gamechanger Grant No. GC 596 (THERMOSIS). Also, the author (BAH) acknowledges the funding support provided by the Leverhulme Trust Research Fellowship (LTRF2021\17131) related to redox hydrothermal reactor for production of green hydrogen.
V.K. would like to thank Dr. Chennakesava Kadapa for the fruitful discussion on thin structures.

REFERENCES

Bansal, N. P. and S. R. Choi (2007). Glass/Ceramic Composites for Sealing Solid Oxide Fuel Cells.

Bansal, N. P., et al. (2007). Glass/BNNT Composite for Sealing Solid Oxide Fuel Cells.

Bingaman, D. C., et al. (2022). A Systems Engineering Approach for the Transition to Zero Emission Aviation. AIAA AVIATION 2022 Forum.

Bradley, M. (2022). Identification and descriptions of fuel cell architectures for aircraft applications. 2022 IEEE Transportation Electrification Conference & Expo (ITEC), IEEE.

Bradley, M. K., et al. (2015). Subsonic ultra green aircraft research.

Choate, A., et al. (2023). NASA's Moon to Mars (M2M) Transit Habitat Refinement Point of Departure Design. 2023 IEEE Aerospace Conference, IEEE.

Faisal, N. H., et al. (2022). "Application of thermal spray coatings in electrolysers for hydrogen production: advances, challenges, and opportunities." ChemNanoMat **8**(12): e202200384.

Faisal, N. H., et al. (2021). "Large-scale manufacturing route to metamaterial coatings using thermal spray techniques and their response to solar radiation." Emergent materials: 1-15.

Goodliff, K. E., et al. (2023). Exploration Systems Development Mission Directorate (ESDMD) Moon-to-Mars Architecture Definition Document, National Aeronautics and Space Administration.

Green, R. D., et al. (2022). "Perspective—solid oxide cell technology for space exploration." Journal of The Electrochemical Society **169**(5): 054528.

Harris, D. W., et al. (2022). Moon to Mars (M2M) Habitation Considerations: A Snap Shot As of January 2022.

Hartvigsen, J., et al. (2018). MOXIE development driven prospects for ISRU and atmosphere revitalization, 48th International Conference on Environmental Systems.

Hwang, M., et al. (2022). "Conceptual design and performance analysis of water electrolysis propulsion system with catalytic igniter for CubeSats." Acta Astronautica **200**: 316-328.

Jakupca, I. (2021). Update on NASA Applications using Solid Oxide Fuel Cell and Electrolysis Technologies. Ohio Fuel Cell Symposium/Solid Oxide Forum.

Karimi, M. and M. Mehrpooya (2022). "Proposal and investigation of a novel hybrid hydrogen production and liquefaction process using solid oxide electrolyzer, solar energy, and thermoelectric generator." Journal of Cleaner Production **331**: 130001.

Kasaeian, A., et al. (2023). "Integration of solid oxide fuel cells with solar energy systems: A review." Applied Thermal Engineering: 120117.

Li, Z., et al. (2021). "Advancing the multiscale understanding on solid oxide electrolysis cells via modelling approaches: A review." Renewable and Sustainable Energy Reviews **141**: 110863.

Meyen, F. E. (2017). System modeling, design, and control of the Mars Oxygen In-Situ Resource Utilization Experiment (MOXIE) and implications for atmospheric ISRU processing plants, Massachusetts Institute of Technology.

Meyen, F. E., et al. (2016). "Thermodynamic model of Mars oxygen ISRU experiment (MOXIE)." Acta Astronautica **129**: 82-87.

Mottaghizadeh, P., et al. (2021). "Dynamics and control of a thermally self-sustaining energy storage system using integrated solid oxide cells for an islanded building." International Journal of Hydrogen Energy **46**(49): 24891-24908.

Mougin, J. (2015). Hydrogen production by high-temperature steam electrolysis. Compendium of Hydrogen Energy, Elsevier: 225-253.

O'Brien, J., et al. (2010). High Temperature Electrolysis for Hydrogen Production from Nuclear Energy–TechnologySummary, Idaho National Lab.(INL), Idaho Falls, ID (United States).

Rostami, M., et al. (2022). "Introducing and evaluation of a new propulsion system composed of solid oxide fuel cell and downstream cycles; usage in unmanned aerial vehicles." International Journal of Hydrogen Energy **47**(28): 13693-13709.

Ryan, A. C., et al. (2013). Air-Independent Solid Oxide Fuel Cells for NASA's LOX-CH4 Landers. Fuel Cell Seminar.

Schmidt, O., et al. (2017). "Future cost and performance of water electrolysis: An expert elicitation study." International Journal of Hydrogen Energy **42**(52): 30470-30492.

Steinetz, B. M., et al. (2004). Solid Oxide Fuel Cell Seal Development at NASA Glenn Research Center. 2004 Fuel Cell Seminar.

Wang, S., et al. (2022). "Numerical assessment of a hybrid energy system based on solid oxide electrolyzer, solar energy and molten carbonate fuel cell for the generation of electrical energy and hydrogen fuel with electricity storage option." Journal of Energy Storage **54**: 105274.

TFAWS23-ID-7

Thermomechanical deformation analysis of a tubular solid oxide steam electrolysis cell

Victoria Kurushina, Vinooth Rajendran,
Anil Prathuru, Mamdud Hossain, Nadimul Faisal
School of Engineering, Robert Gordon University,
Aberdeen, AB10 7GJ, UK

Ajith Soman, Bahman Amini Horri, Qiong Cai
University of Surrey, University Campus, Guildford,
GU2 7XH, UK

ROBERT GORDON UNIVERSITY ABERDEEN
UNIVERSITY OF SURREY
UKRI Engineering and Physical Sciences Research Council

Thermal & Fluids Analysis Workshop TFAWS 2023
August 21-25, 2023
NASA Goddard Space Flight Center College Park, MD

Contents

Introduction to SOE

Solid oxide steam electrolysis explained

1 Steam supply at high temperature into the gas channel and splitting into ions of oxygen and hydrogen at the cathode

$$H_2O \rightarrow 2H^+ + O^{2-}$$

2 Cations of hydrogen gain electrons at the cathode, powered by the external electrical circuit, and the formed molecules of hydrogen leave the gas channel at the outlet, mixed with the remainder steam

$$2H^+ + 2e^- \rightarrow H_2$$

3 Anions of oxygen pass through the electrolyte (membrane/solution), attracted by the anode, where they loose extra electrons and form zero-valence molecules that exit the gas channel

$$O^{2-} - 2e^- \rightarrow O_2$$

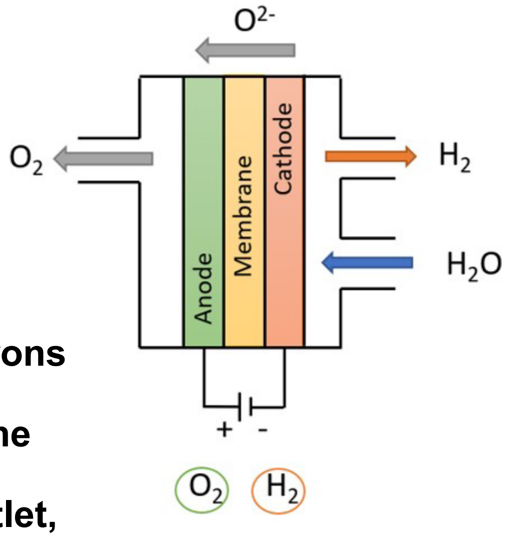

Uses of H_2?

- Refining petroleum
- Treating metal
- Producing fertiliser
- Processing foods
- Energy storage and producing electricity for a wide variety of devices and vehicles
- Burning hydrogen blended with natural gas

Uses of O_2?

- Part of breathable air for life support
- As oxidizer, for propulsion, welding, cutting
- For medical applications

Introduction to SOE

Water electrolysis technologies

Dominant technologies:

- *proton exchange membrane electrolysis cells* (PEMEC);
- anion exchange membrane electrolysis cells (AEMEC);
- *alkaline water electrolysis cells* (AWEC);
- *solid oxide steam electrolysis cells* (SOSEC);
- thermochemical water splitting (TWS);
- photolysis water splitting (PWS);
- photoelectrochemical water electrolysis cells (PECWEC).

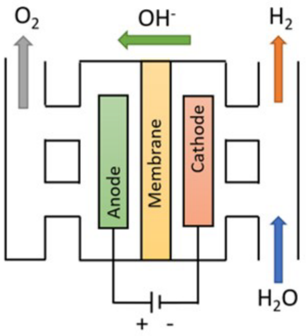

PEMEC – mature

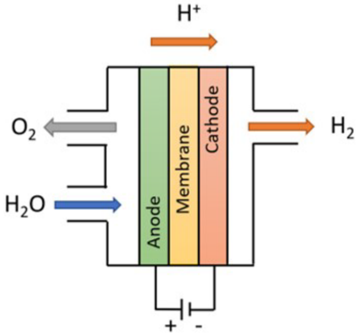

AWEC – commercial

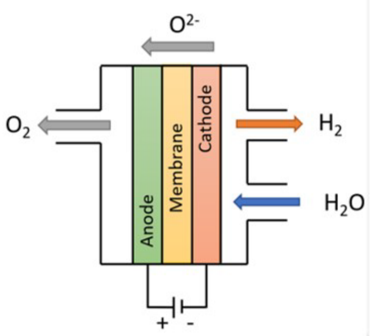

SOSEC – demonstration

Characteristics	Units	PEMEC	AEC	SOEC
Operating temperature	°C	50-80	60-80	650-1000
Current density	A/cm^2	0.6-2.0	0.2-0.4	0.3-2.0
Cell voltage	V	1.8-2.2	1.8-2.4	0.7-1.5
Operating pressure	bar	< 200	< 30	< 25
Production rate	m^3/h	< 40	< 760	< 40
Stack lifetime	hours	20 000 - 60 000	60 000 - 90 000	10 000
Stack energy	kWh/m^3	4.2-5.5	4.2-5.9	>3.2
Capital cost	euro/kW	1 860 - 2 320	1 000 - 1 200	> 2 000

SOE efficiency and advantages

- Higher temperature leads to better performance due to reduction in anode and cathode activation overpotential.
- However, it creates thermal stress and less durable cells.

Current challenges

1. Costs should be reduced for all stages of the stack lifecycle.
2. Material degradation accelerated in high temperature conditions.
3. Fabrication of cells, production of complex materials may not be completely clean.
4. Lack of commercialization.
5. Lack of manufacturing innovations.

Advantages

1. High efficiency and controllability of reaction rates is achievable in high temperature conditions.
2. Combined input of thermal and electrical energy makes it compatible with wide range of systems with either type of excess energy.
3. SOEC, SOFC and reversible cells are well suited for intermittent operation.
4. Use of solid materials for the functional layers simplifies transportation, installation and operation.
5. SOEC operation is environmentally friendly.
6. Produced hydrogen is free from contaminants.

Introduction to SOE

SOE integration

- Heat
- Electricity
- Feedstock materials

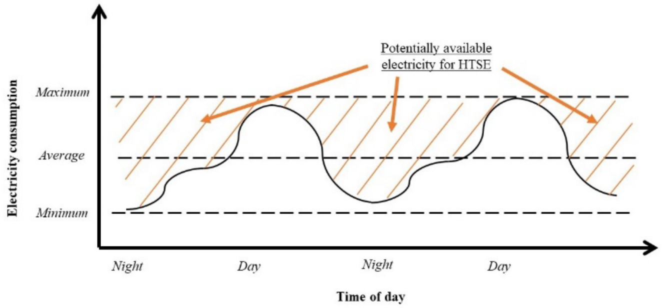

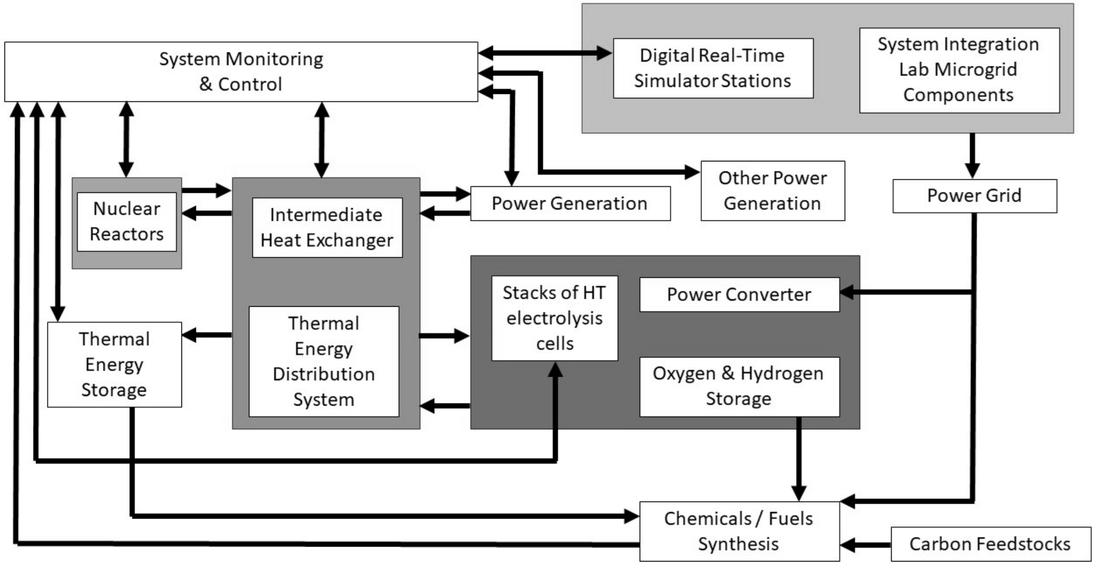

System Monitoring & Control

Digital Real-Time Simulator Stations

System Integration Lab Microgrid Components

Nuclear Reactors

Intermediate Heat Exchanger

Power Generation

Other Power Generation

Power Grid

Stacks of HT electrolysis cells

Power Converter

Thermal Energy Storage

Thermal Energy Distribution System

Oxygen & Hydrogen Storage

Chemicals / Fuels Synthesis

Carbon Feedstocks

Integration potential:

- ❑ Nuclear plants
- ❑ Solar plants
- ❑ Wind farms
- ❑ Hybrid energy systems
- ❑ Aviation
- ❑ Spacecraft systems, etc.

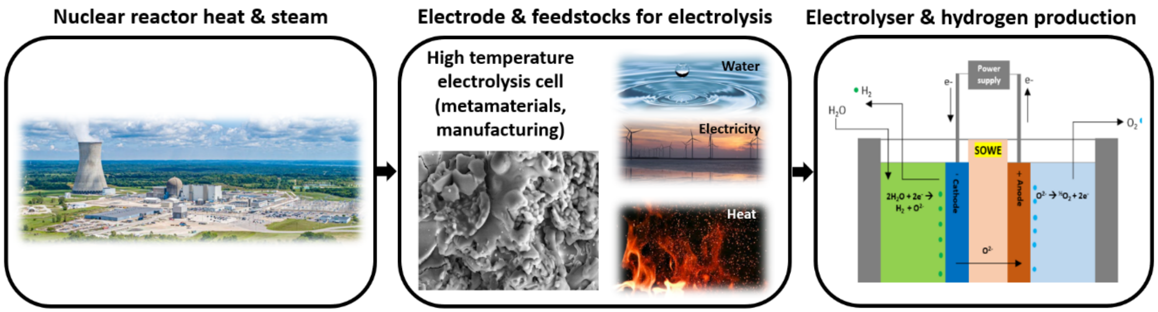

Nuclear reactor heat & steam

Electrode & feedstocks for electrolysis

Electrolyser & hydrogen production

High temperature electrolysis cell (metamaterials, manufacturing)

Introduction to SOE

SOE modelling

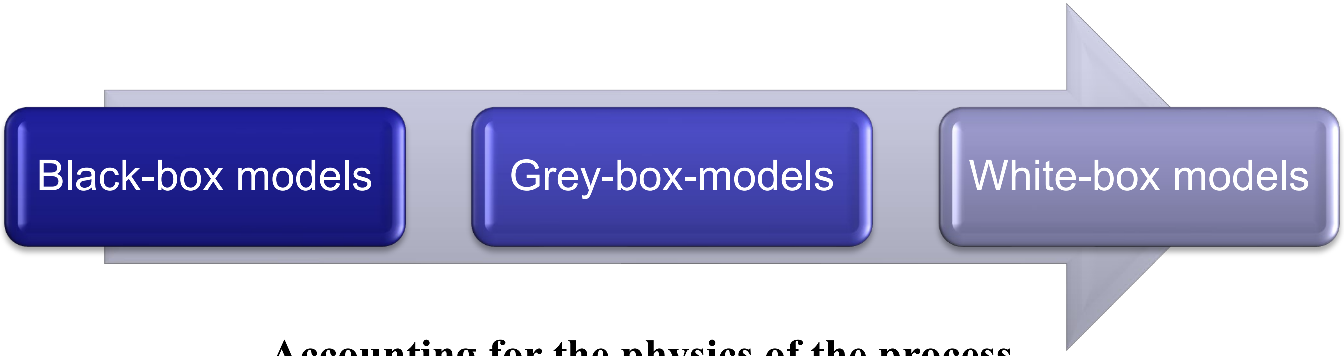

Black-box models

Grey-box-models

White-box models

Accounting for the physics of the process

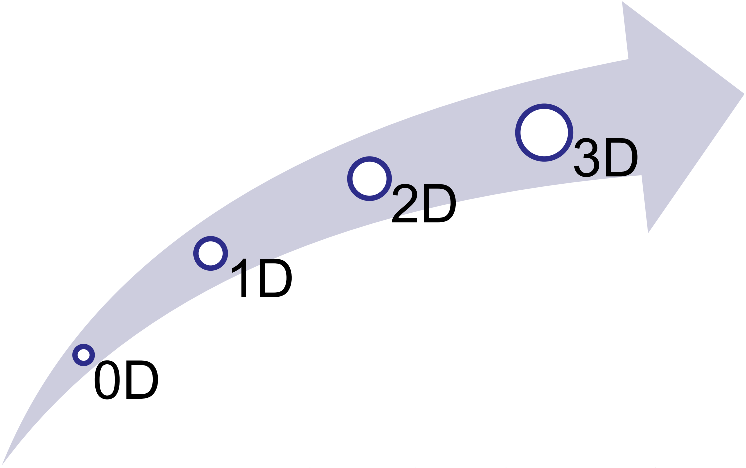

0D

1D

2D

3D

Model dimensionality (spatial)

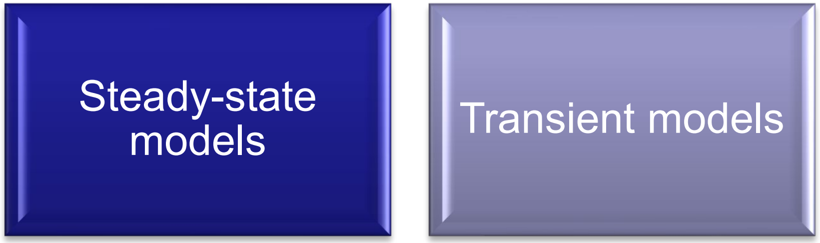

Steady-state models

Transient models

Model dimensionality (temporal)

Introduction to SOE

SOE modelling

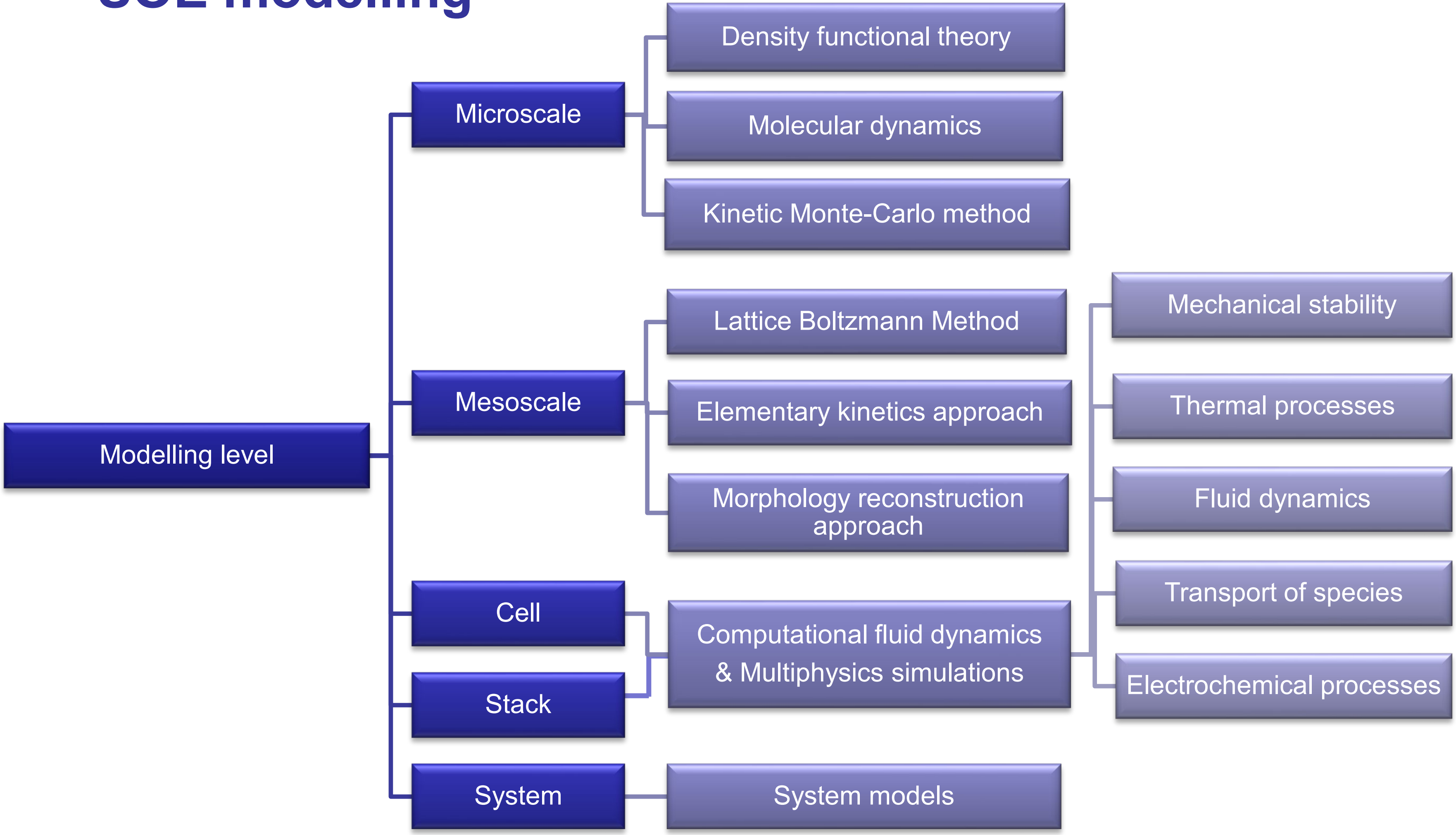

- Modelling level
  - Microscale
    - Density functional theory
    - Molecular dynamics
    - Kinetic Monte-Carlo method
  - Mesoscale
    - Lattice Boltzmann Method
    - Elementary kinetics approach
    - Morphology reconstruction approach
  - Cell
  - Stack
    - Computational fluid dynamics & Multiphysics simulations
      - Mechanical stability
      - Thermal processes
      - Fluid dynamics
      - Transport of species
      - Electrochemical processes
  - System
    - System models

Introduction to SOE

SOE cell designs

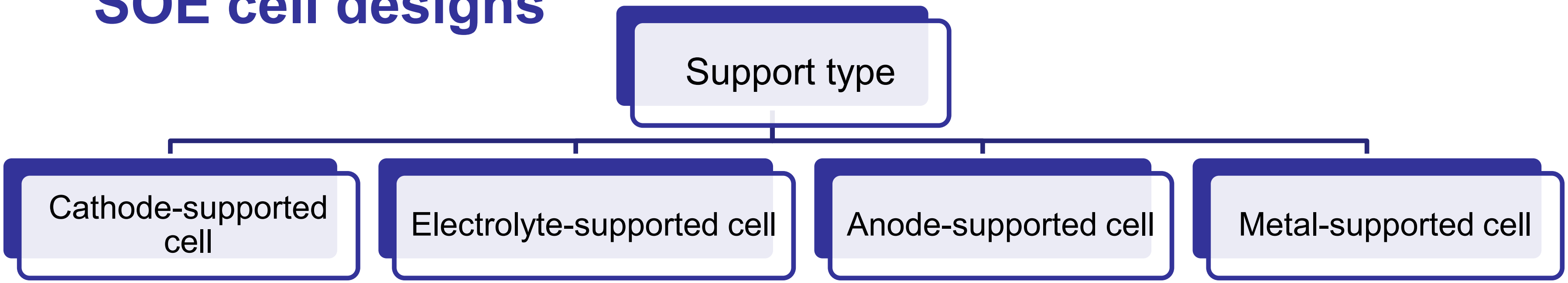

Support type

Cathode-supported cell

Electrolyte-supported cell

Anode-supported cell

Metal-supported cell

Thick cathode	Thick electrolyte	Thick anode	Thick metal
+ Good cell stability during electrochemical process - High resistance for polarization	+ High mechanical robustness + Good gas diffusion properties - High ohmic losses in the thickened electrolyte layer	+ Lower operating temperature + Low ohmic resistance + Lower costs of material + Considered to be easier for fabrication - Lower mechanical reliability	+ High mechanical stability - Energy losses in the supporting porous metal layer

Project overview

Objectives

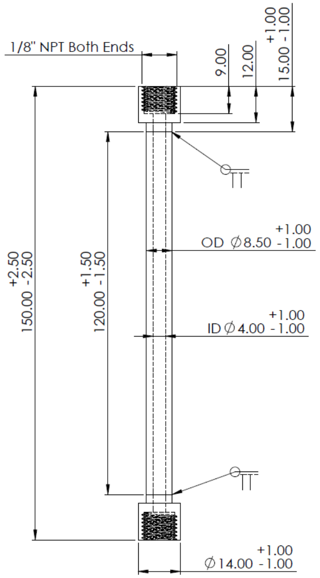

- Development of large-scale and hierarchical length scale cathode catalyst layer (tubular metasurface) using thermal spray coating technique (using air plasma spray) for an enhanced structurally stable SOSE cell design;
- Development of a customised SOSE cell design with a tubular electrode assembly for an integration with high temperature steam line (with higher thermo-mechanical and electro-chemical performance and long-term structural stability).

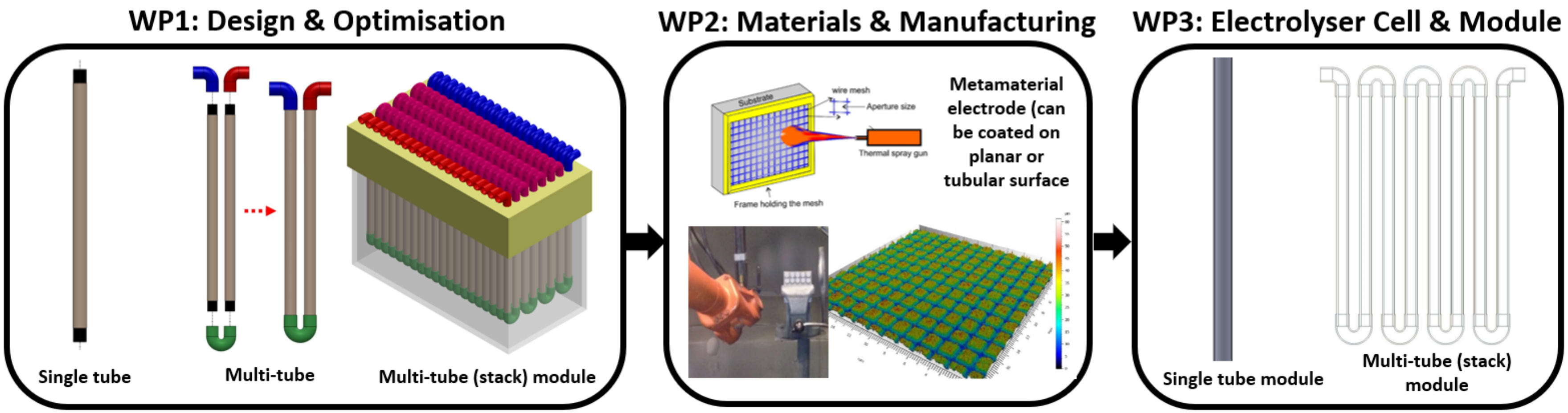

Fig. 1 METASIS methodology.

Project overview

Work packages

- **WP1 (Electrolyser design and optimisation)**
  - Task 1.1. Benchmarking of electrolyser
  - Task 1.2. Structural analysis
  - Task 1.3. Computational fluid dynamics

- **WP2 (Materials selection, manufacturing, and electrode cell development)**
  - Task 2.1 Materials selection and processing
  - Task 2.2. Electrode materials comparison

- **WP3 (Scaled manufacturing of electrolyser cell with metasurface design)**
  - Task 3.1. Manufacturing of tubular electrode with metasurface cathode
  - Task 3.2. Prototype testing and validation

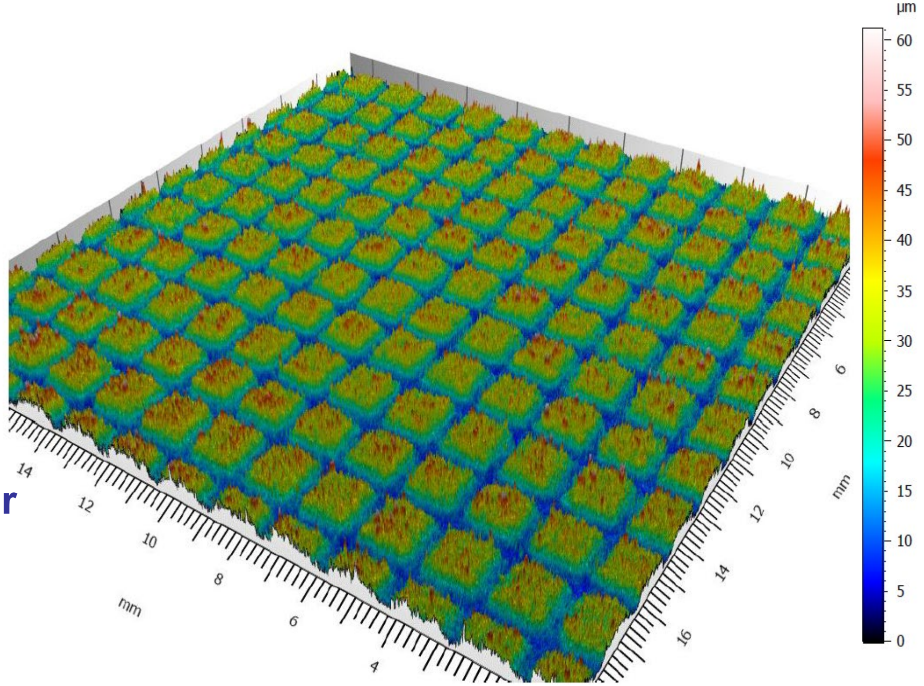

Project overview

METASIS experimental tests

Our targets

- Improving efficiency
- Lower cost
- Durability
- Scalability & system integration

<u>Material characterization</u> tests to be performed in the Robert Gordon University

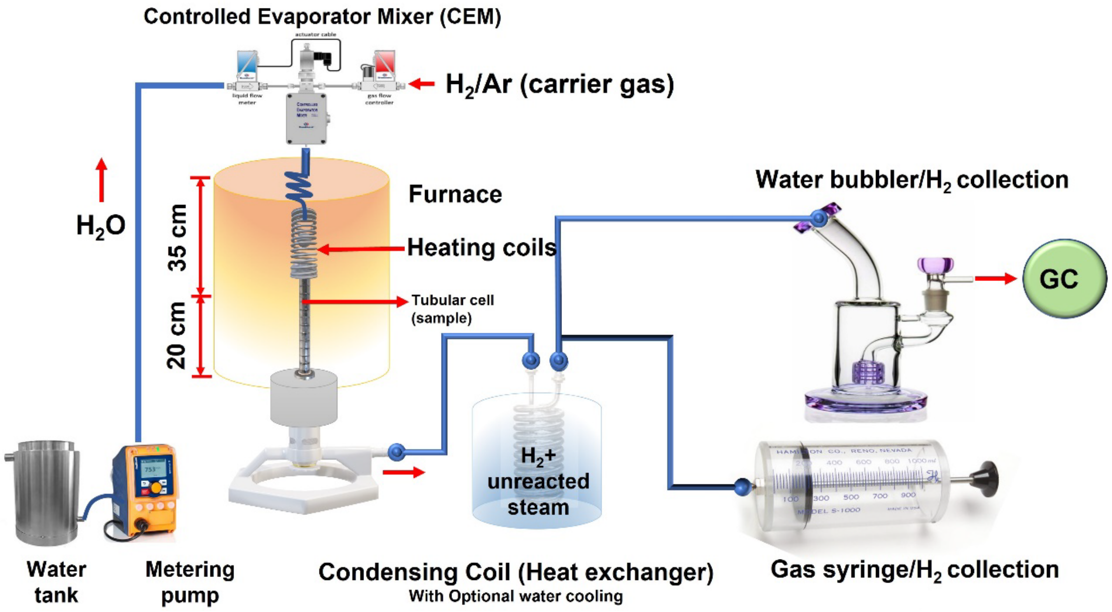

<u>High temperature</u> tests to be performed in the University of Surrey

Thermomechanical model

Tubular cell design and composition

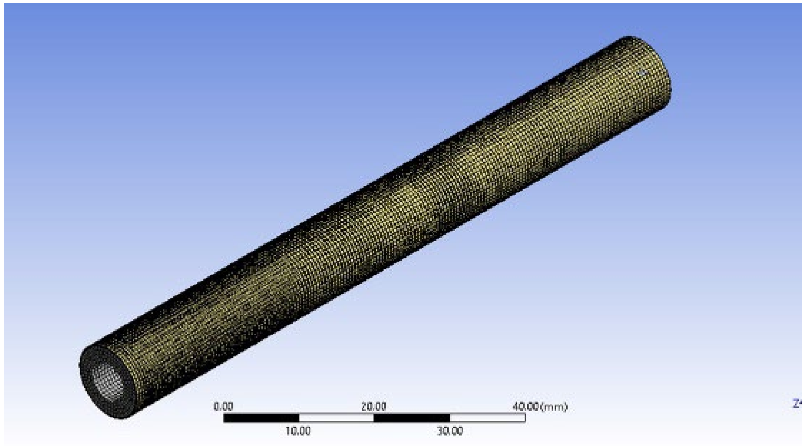

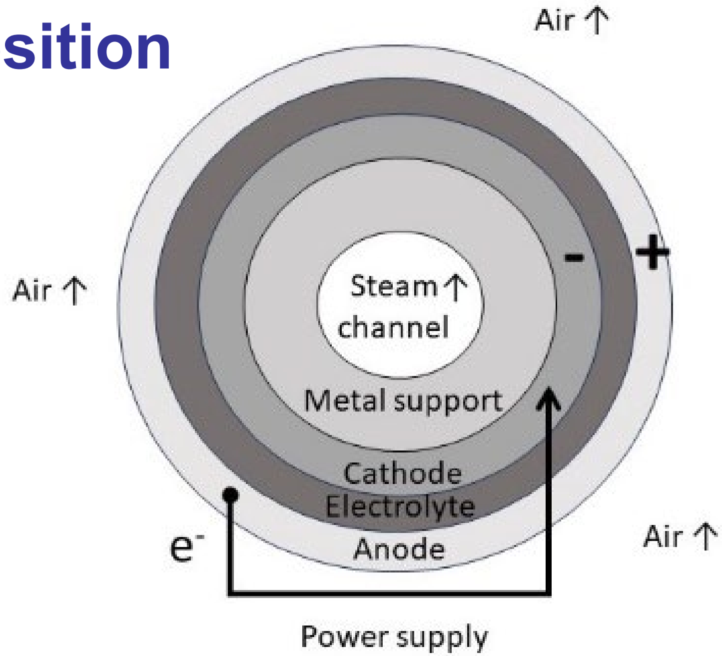

Layer	Functionality	Thickness (per design), mm	Material	Proposed manufacturing technique	Porosity (per design), %
1	Substrate	2.150	Titanium alloy	Commercial	30
2	Interconnect	0.035	Silver	Electrodeposition	0
3	Cathode	0.070	Nickel oxide and GDC	Dip coating / Thermal spray	30
4	Electrolyte	0.022	GDC and YSZ	Dip coating	0
5	Anode	0.070	GDC and LSCF	Dip coating / Thermal spray	30
6	Interconnect	0.035	Silver	Wire wrapped around the cell	30

Thermomechanical model

Tubular cell design and composition

Material	Density, kg/m^3	Melting temperature, °C	Young's modulus, GPa	Poisson ratio	Thermal expansion coefficient, µm/m·°C	Tensile yield strength, MPa	Ultimate yield strength, MPa
Titanium alloy	4405	1370	107	0.32	8.9	850	1098
Silver	10500	961	83	0.37	19	54	140
Nickel oxide	4670	1605	160	0.26	12.5	440	646
GDC	7200	2600	120	0.26	11.5	1.95	200
YSZ	5900	2700	210	0.28	10.5	750	1200
LSCF	6000	920	170	0.30	14.5	94	160

Property	Units	Cathode	Electrolyte	Anode
Density	kg/m^3	5682	7082	6600
Melting point	°C	2003	2609	1760
Young's modulus	GPa	144	128	145
Poisson's ratio		0.26	0.26	0.28
Thermal expansion coefficient	µm/m·°C	12.1	11.4	13
Tensile yield strength	MPa	265	24.5	48
Ultimate yield strength	MPa	467	223	180

Thermomechanical model

Model set-up

- Standard solid elements for the substrate
- Shell elements for five functional layers
- Full tube of 100 mm length and 6 mm internal diameter
- Bonded contacts set between the layers
- The sixth layer is assumed to be a layer of a uniform material

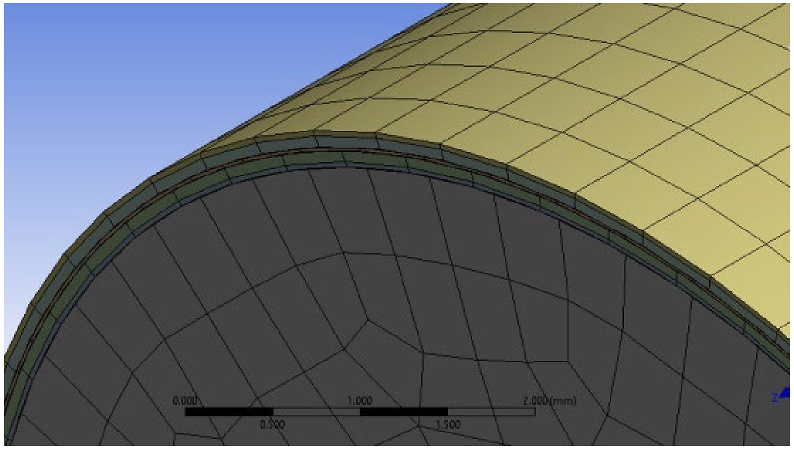

#	Number of cells	Maximum total deformation of the outer silver interconnect, mm	Maximum total deformation of the titanium substrate, mm
1	22 537	0.10441	0.079562
2	37 862	0.11159	0.078981
3	50 962	0.11234	0.078593
4	76 192	0.11036	0.078641
5	**90 762**	**0.088686**	**0.078468**
6	118 342	0.094807	0.078269
7	129 009	0.087868	0.079190
8	141 911	0.089302	0.078229

Base case == worst case of the thermal expansion in the middle of the temperature range:

- **Fixed-fixed connections**
- **No porosity**
- **800 °C thermal load**
- **1 MPa internal pressure**

Results

Stress analysis for 800 °C

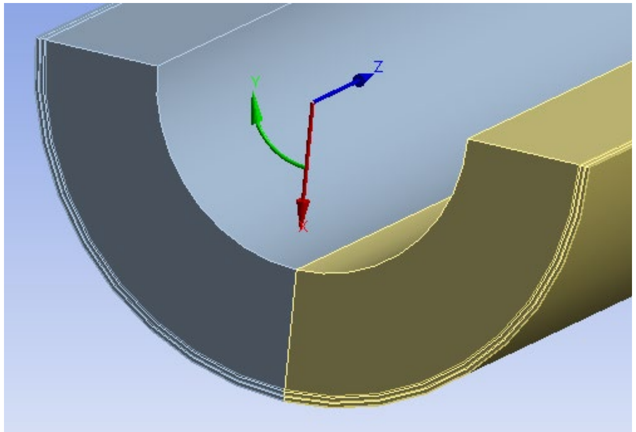

Cylindrical coordinate system

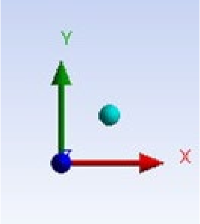

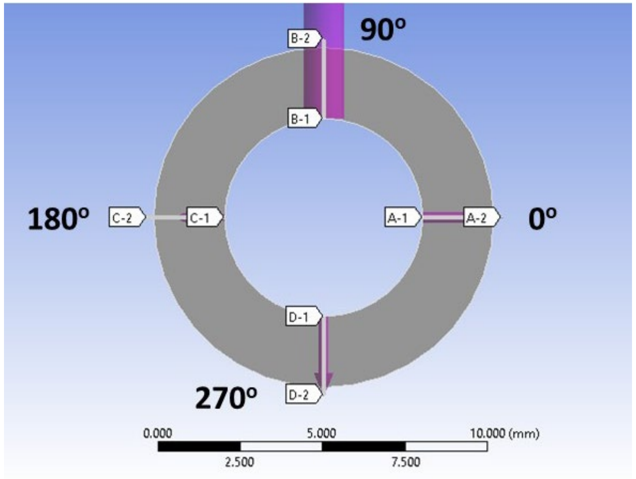

Locations of cross-section cuts

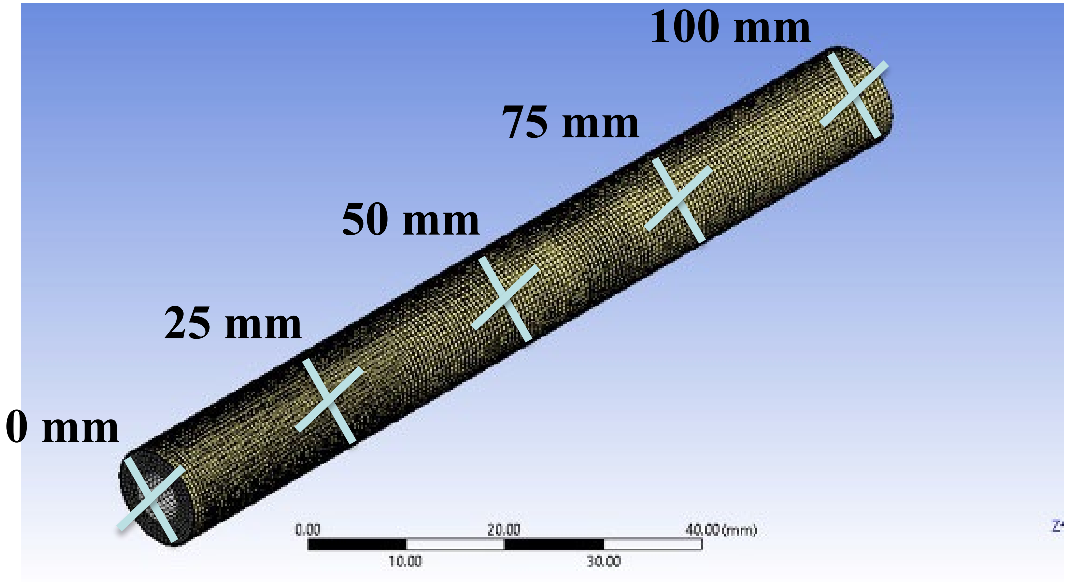

Location of representative cross-sections

Results

Stress analysis for 800 °C

Max total deformation 0.0887 mm

- View from the X axis
- Fixed-fixed boundary conditions
- Porosity 0%

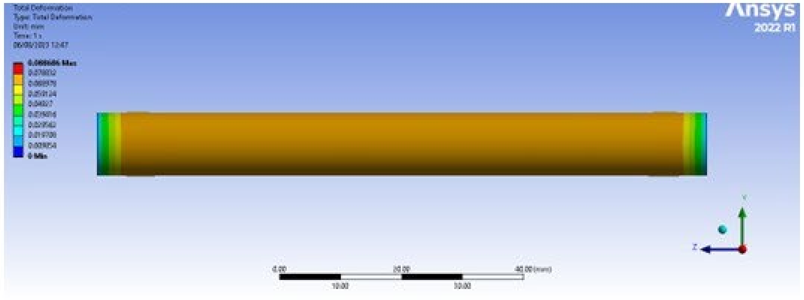

Layer 1

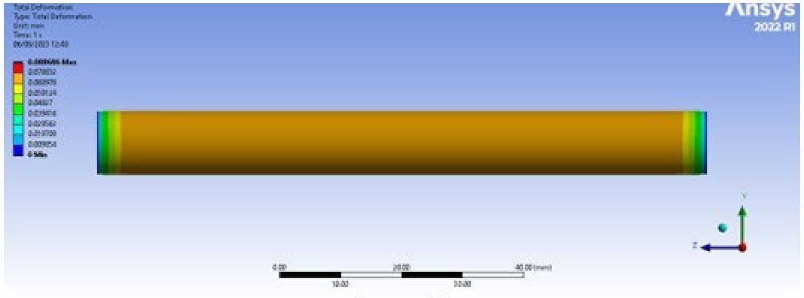

Layer 2

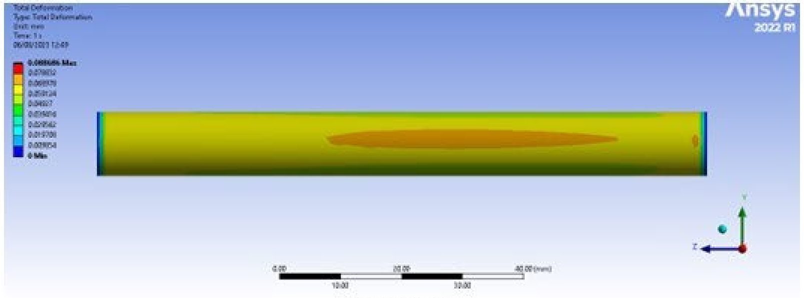

Layer 3

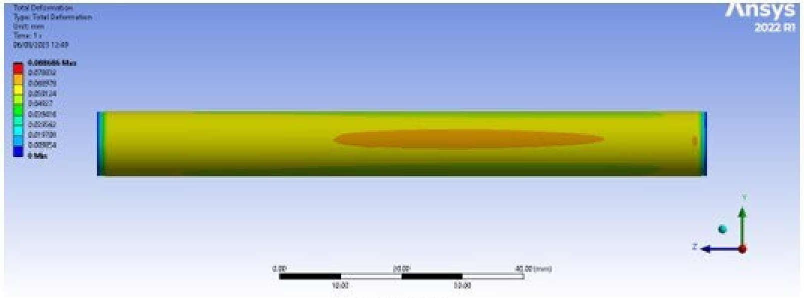

Layer 4

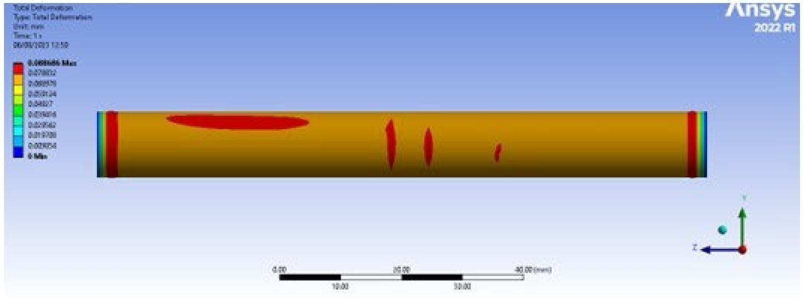

Layer 5

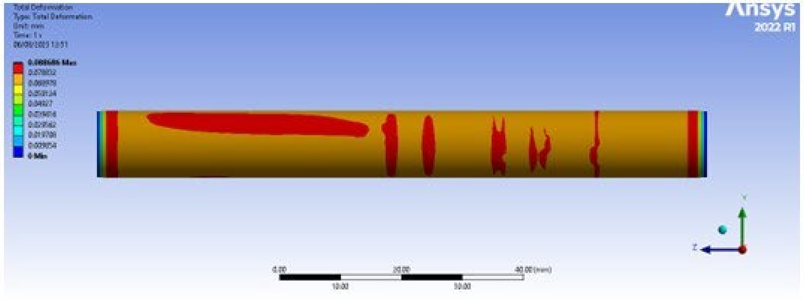

Layer 6

Results

Stress analysis for 800 °C

Max total deformation 0.0887 mm

- ➢ **View from the Y axis**
- ➢ **Fixed-fixed boundary conditions**
- ➢ **Porosity 0%**

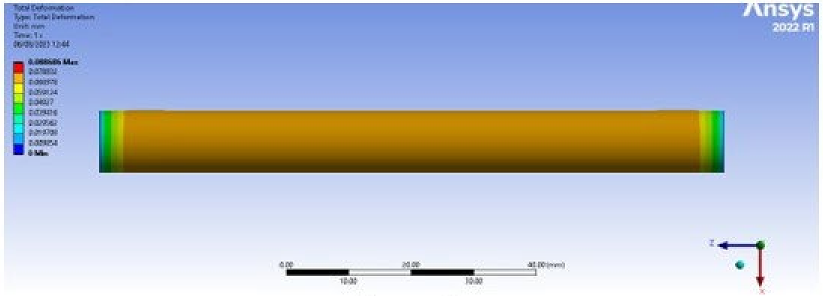

Layer 1

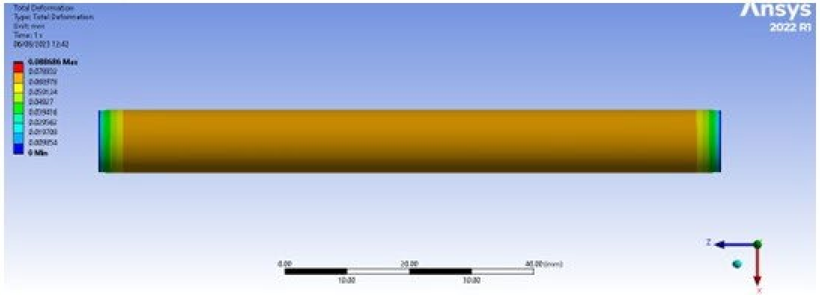

Layer 2

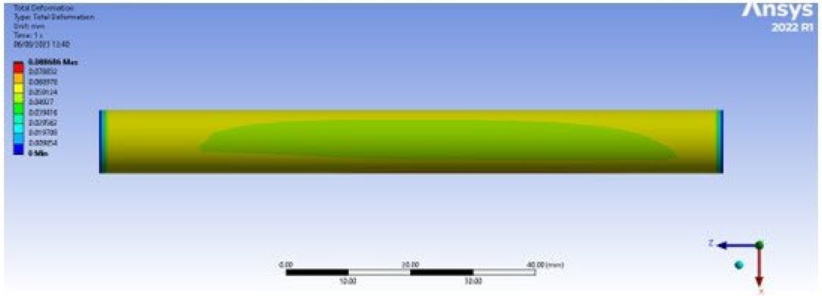

Layer 3

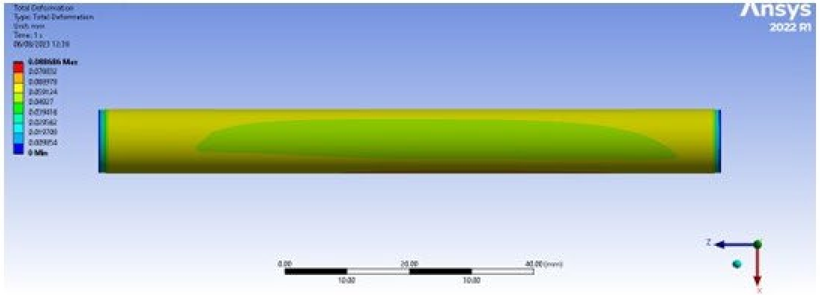

Layer 4

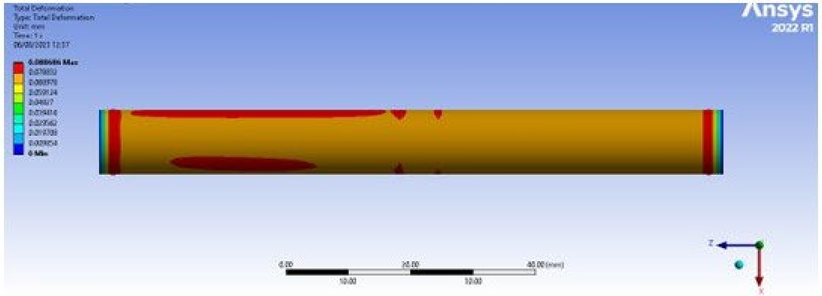

Layer 5

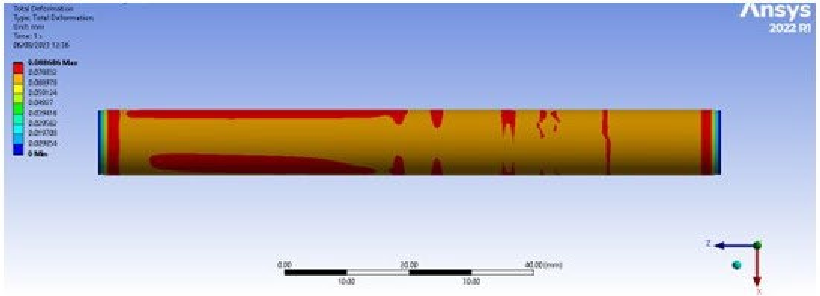

Layer 6

Results

Stress analysis for 800 °C

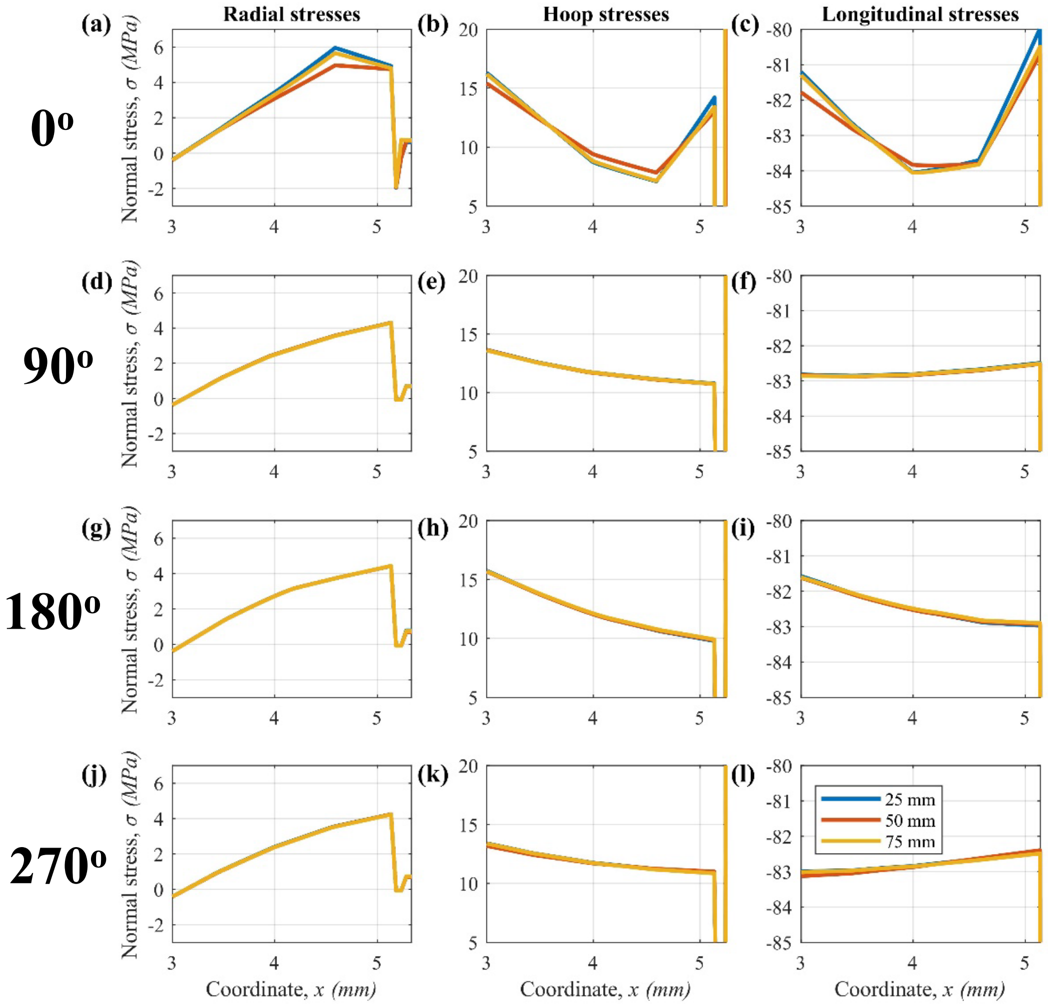

Max total deformation 0.088686 mm

- **Normal stresses observed with fixed-fixed boundaries – enlarged for comparison**
- **Porosity 0%**

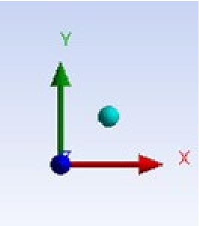

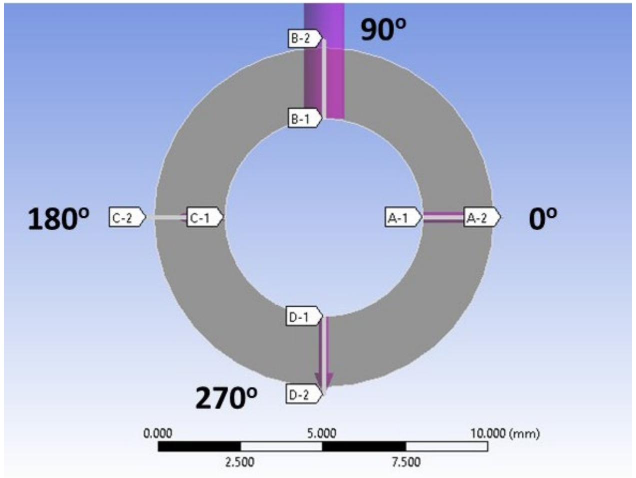

Orientation cross-section cuts

Results

Effect of boundary conditions

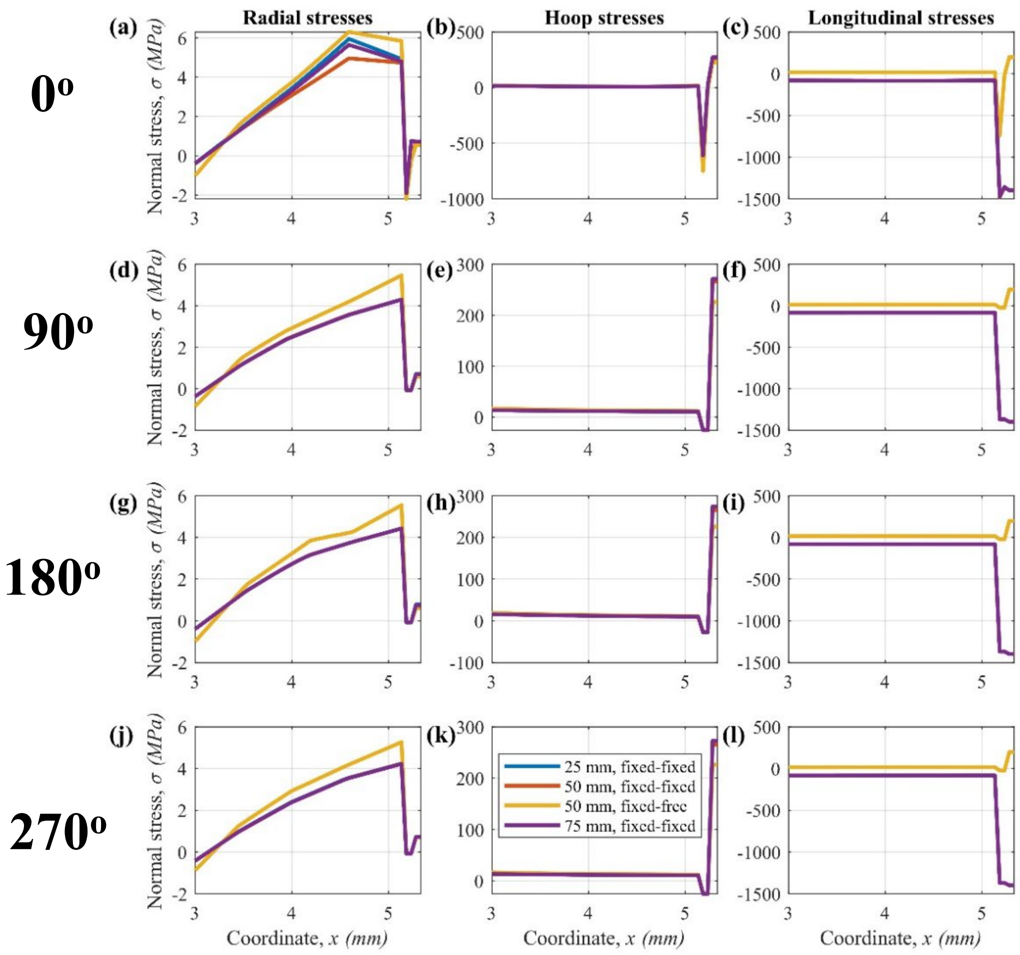

Max total deformation
0.088686 mm vs. 1.1293 mm

- **Normal stresses in comparison for fixed-fixed and fixed-free boundary conditions – full scale**
- **Porosity 0%**
- **Temperature 800 °C**

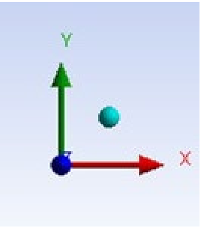

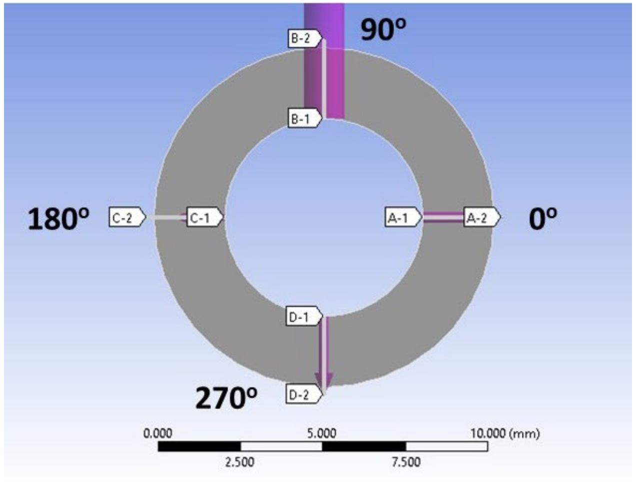

Orientation cross-section cuts

Results

Effect of boundary conditions

- ➤ **Total deformation at fixed-free conditions**
- ➤ **Temperature 800 ^{o}C**
- ➤ **Porosity 0%**

Max total deformation 1.1293 mm

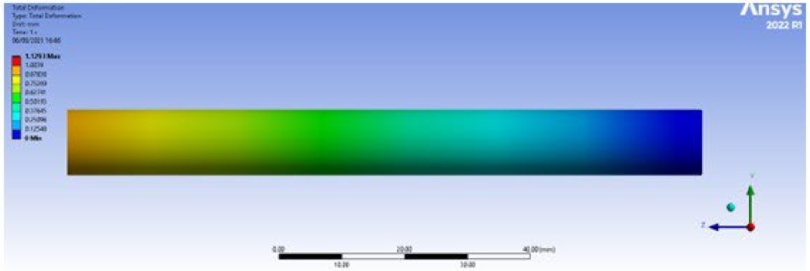

Layer 1

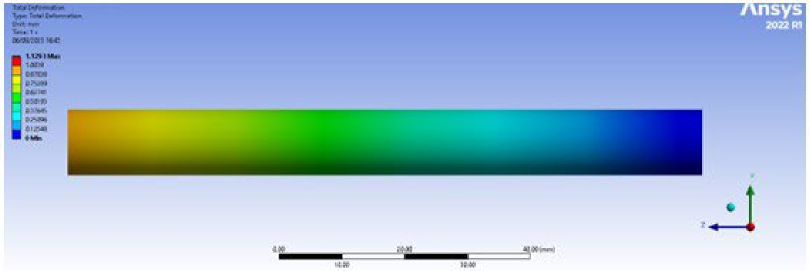

Layer 2

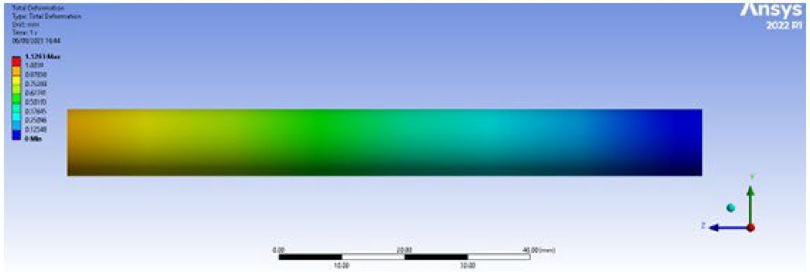

Layer 3

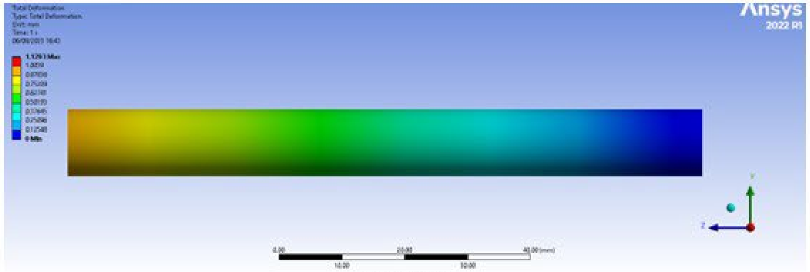

Layer 4

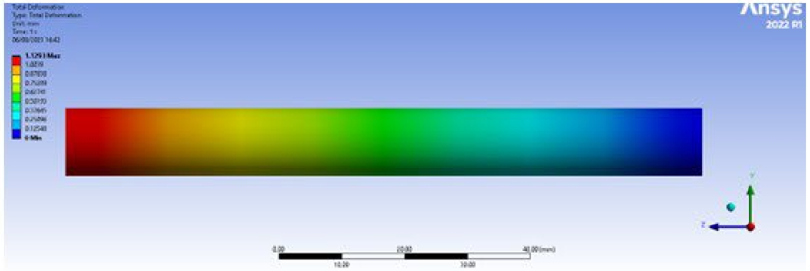

Layer 5

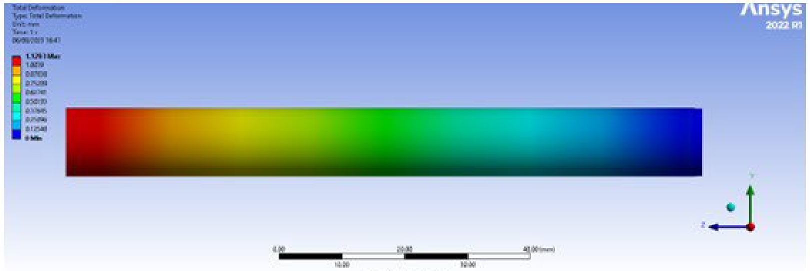

Layer 6

Results

High temperature effects

- ➢ Temperature 1000 ^{o}C
- ➢ Fixed-fixed boundary conditions
- ➢ View from X axis
- ➢ Porosity 0%

Largest max total deformation observed at these B.C. – 0.1115 mm

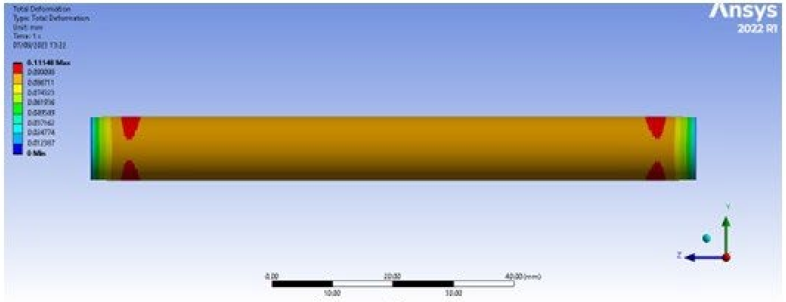

Layer 1

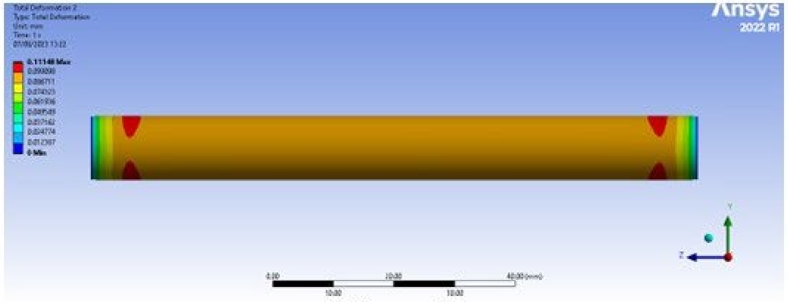

Layer 2

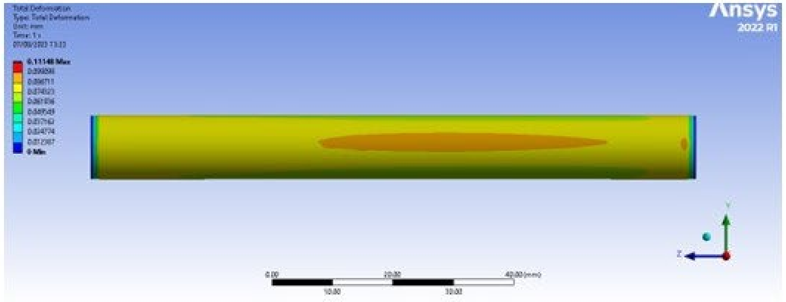

Layer 3

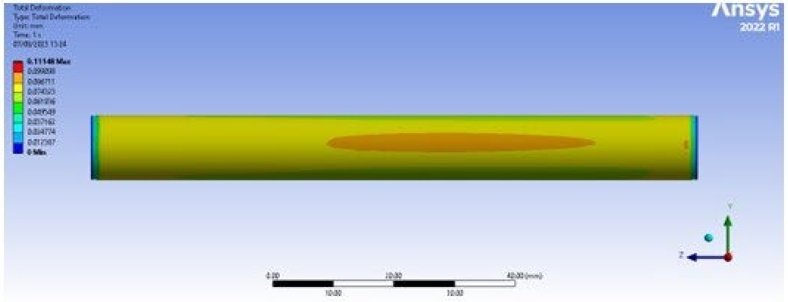

Layer 4

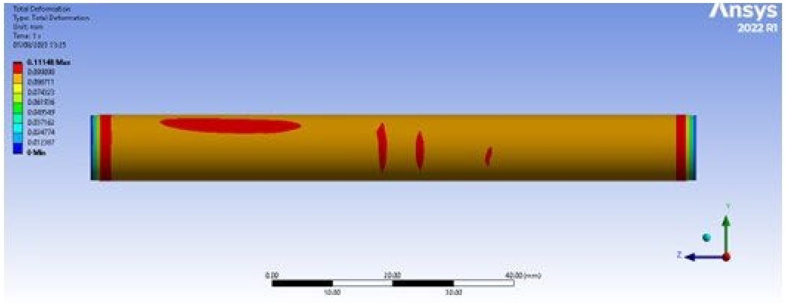

Layer 5

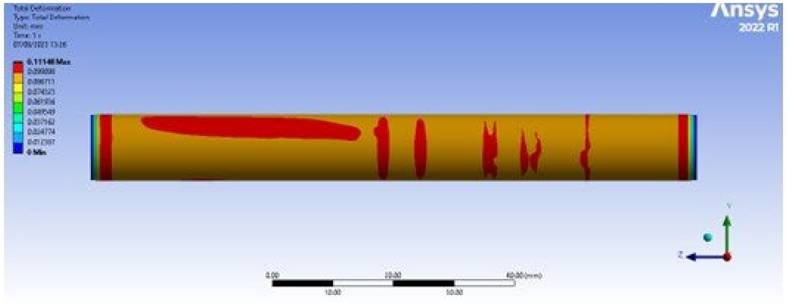

Layer 6

Results

High temperature effects

- ➢ Temperature 1000 °C
- ➢ Fixed-fixed boundary conditions
- ➢ View from Y axis
- ➢ Porosity 0%

Largest max total deformation observed at these B.C. – 0.1115 mm

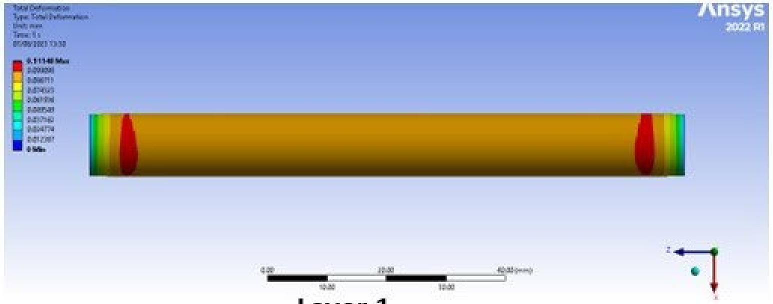

Layer 1

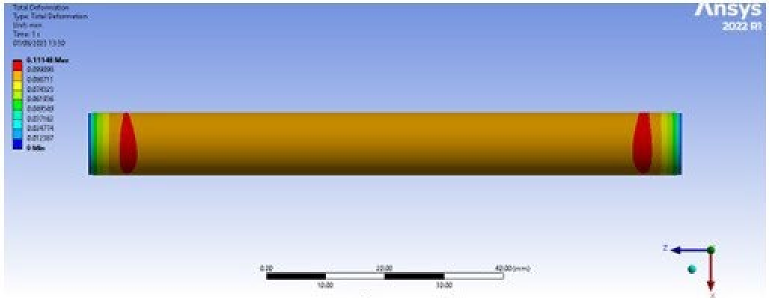

Layer 2

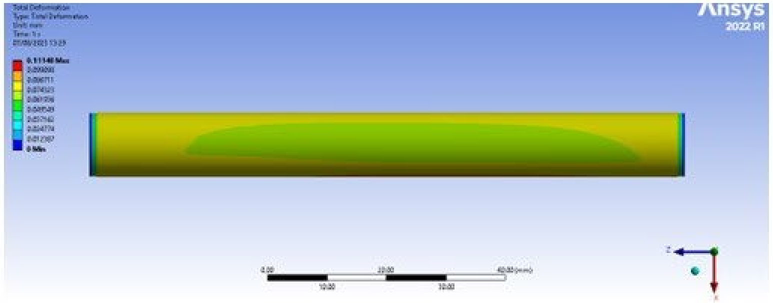

Layer 3

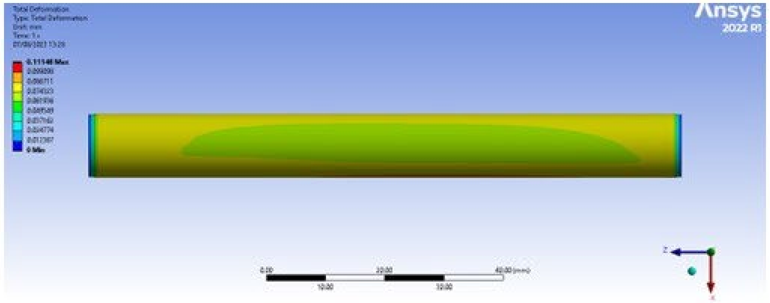

Layer 4

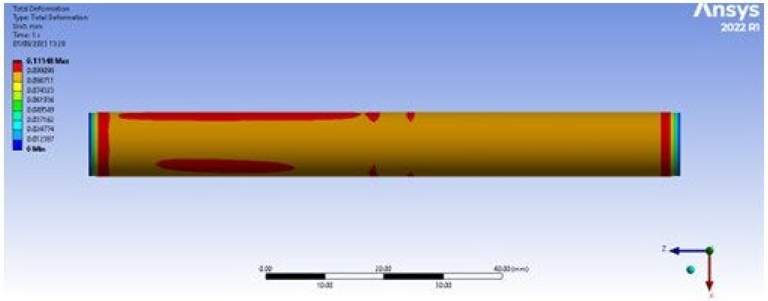

Layer 5

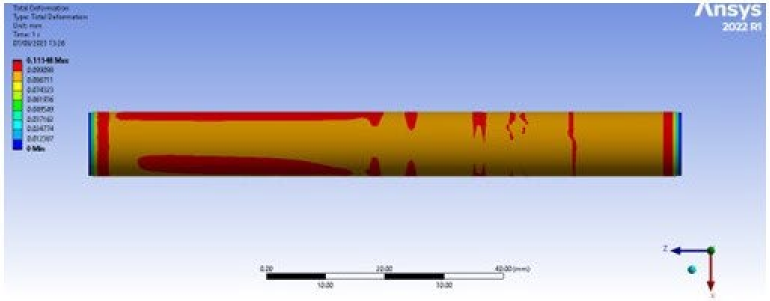

Layer 6

Results

- Fixed-fixed conditions

High temperature effects

Maximum total deformation of the outer layer

The same porosity in all layers

Porosity in layers 1, 3, 5, 6, according to the design

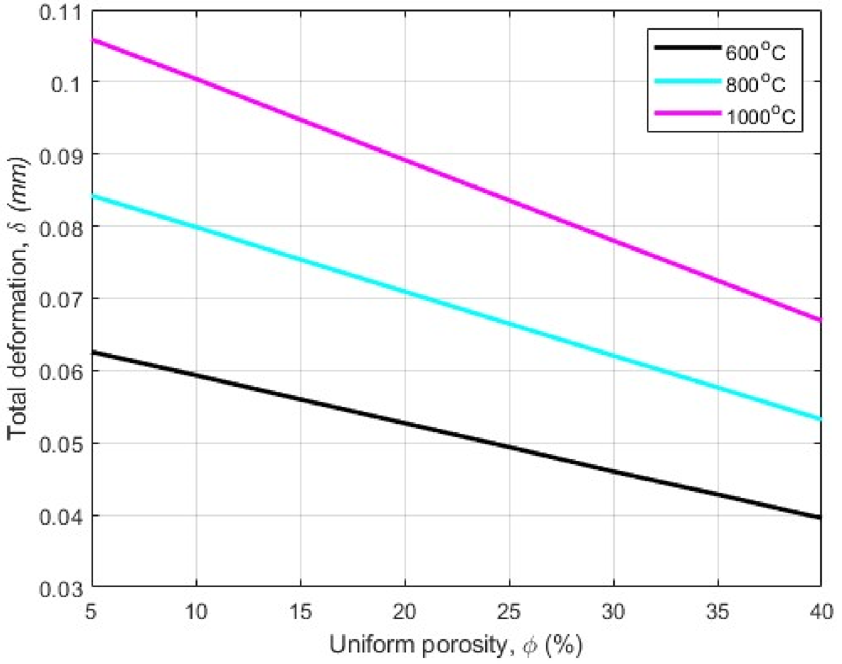

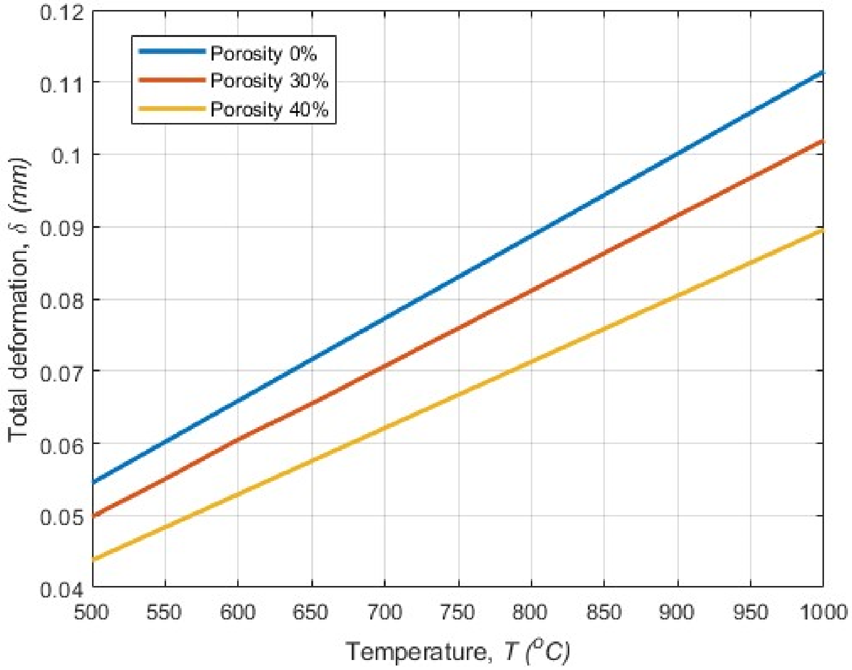

Effect of the change in CTE of the electrolyte layer (layer 4)

Results

High temperature effects

- ➢ Fixed-fixed boundary conditions
- ➢ Middle cross-section at 0^{o}

Radial stress **Hoop stress** **Longitudinal stress**

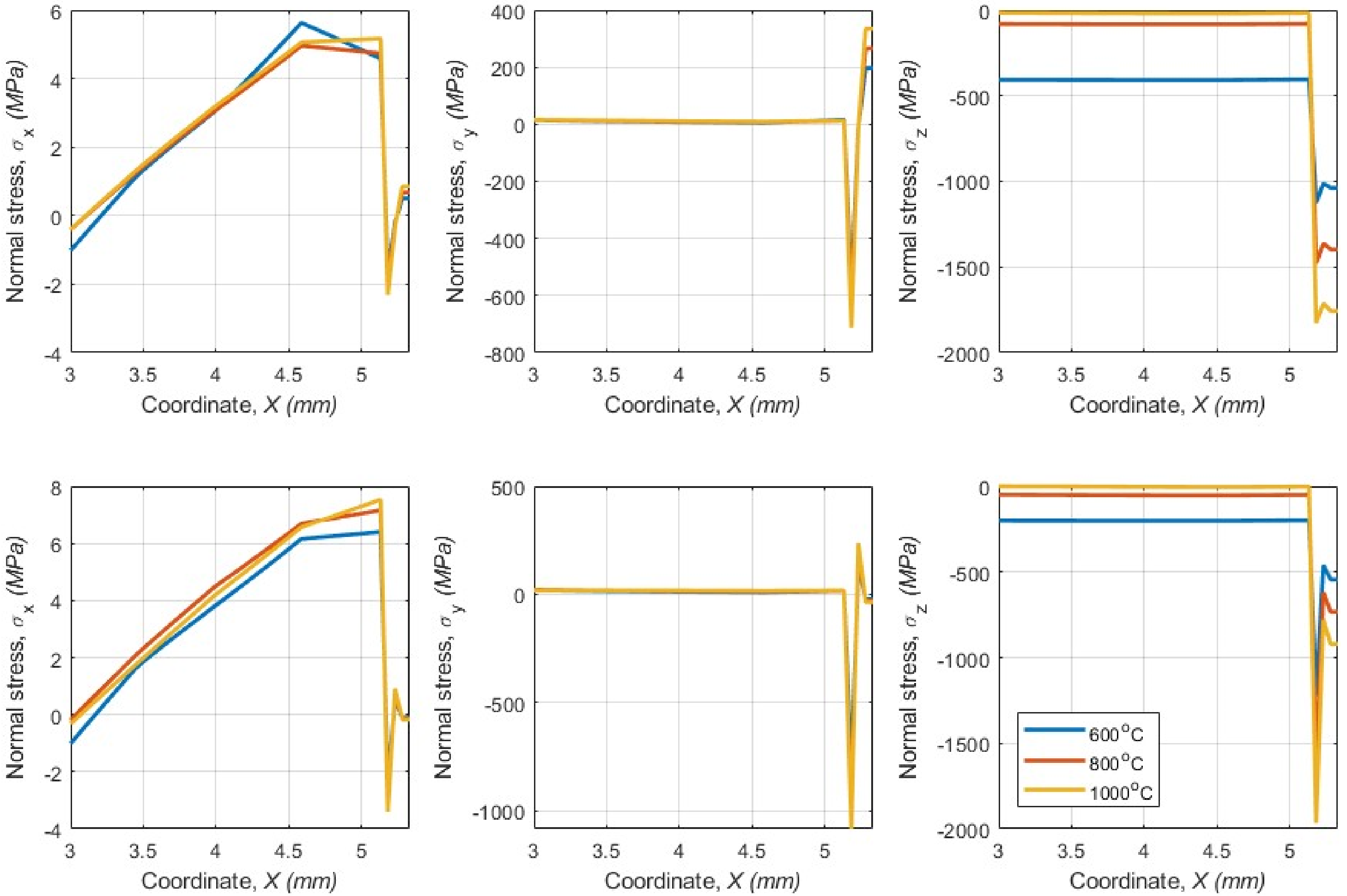

Porosity 0%

Design porosity 30% in layers 1, 3, 5, 6

Results

Effect of porosity

Max total deformation 0.0811 mm

- Total deformation with the designed 30 % porosity in layers 1, 3, 5, 6
- Temperature 800 ^oC

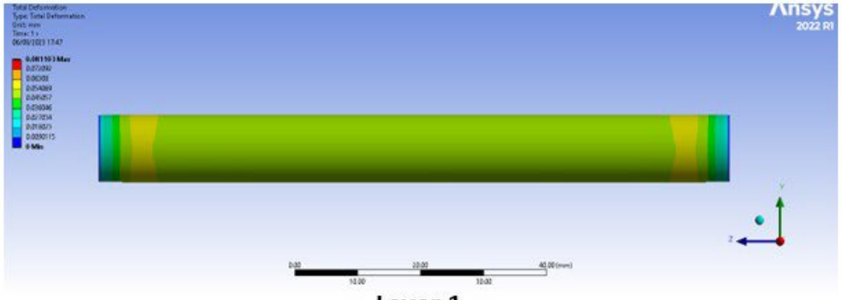

Layer 1

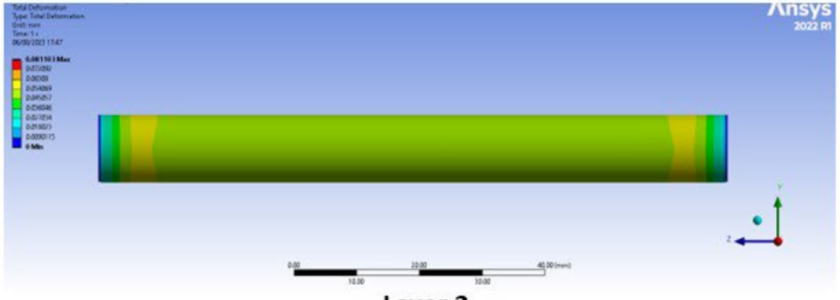

Layer 2

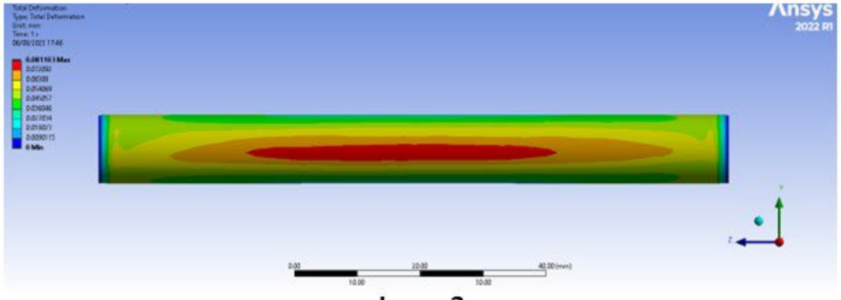

Layer 3

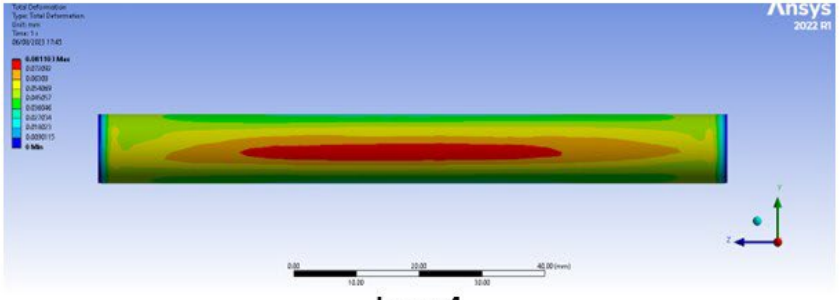

Layer 4

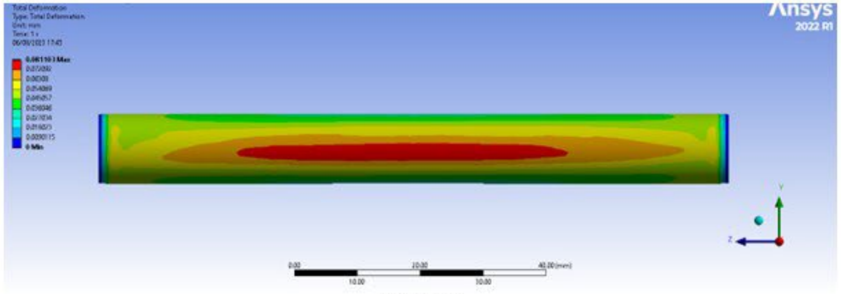

Layer 5

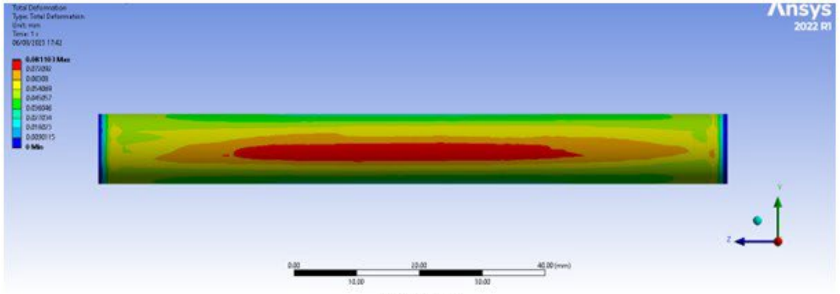

Layer 6

Results

Effect of porosity

Max total deformation 0.0713 mm

- ➢ **Total deformation with the 40 % porosity in layers 1, 3, 5, 6**
- ➢ **Temperature 800 ^{o}C**

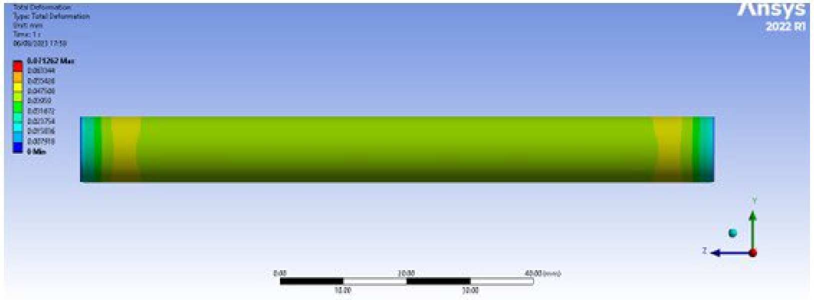

Layer 1

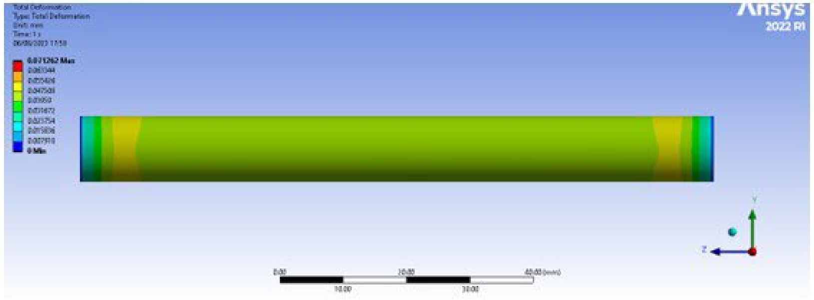

Layer 2

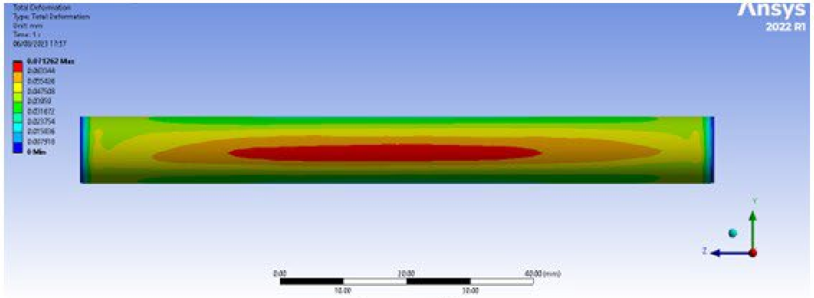

Layer 3

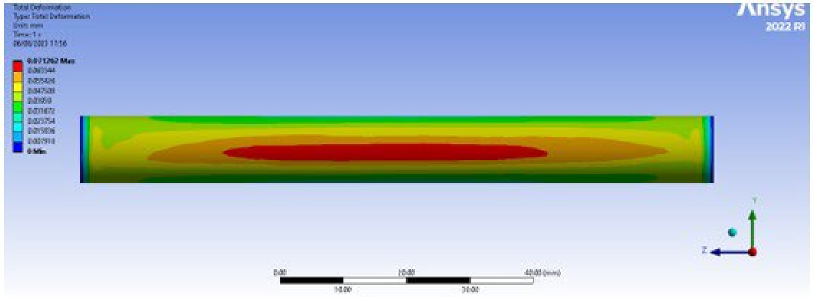

Layer 4

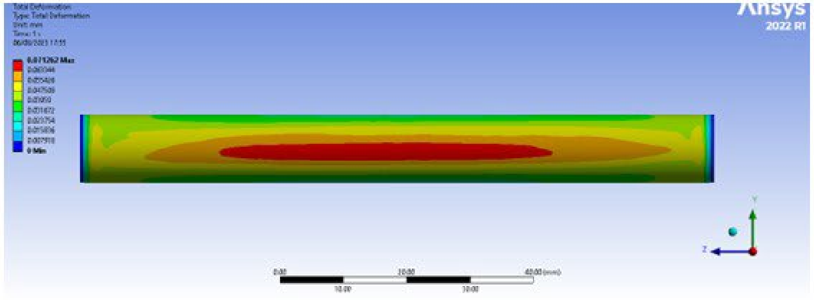

Layer 5

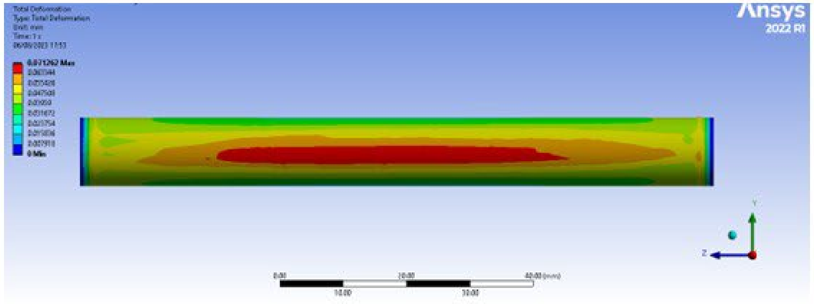

Layer 6

Results

Effect of porosity

- ➢ Fixed-fixed boundary conditions
- ➢ Temperature 800 ^{o}C
- ➢ Middle cross-section at 0^o

Radial stress **Hoop stress** **Longitudinal stress**

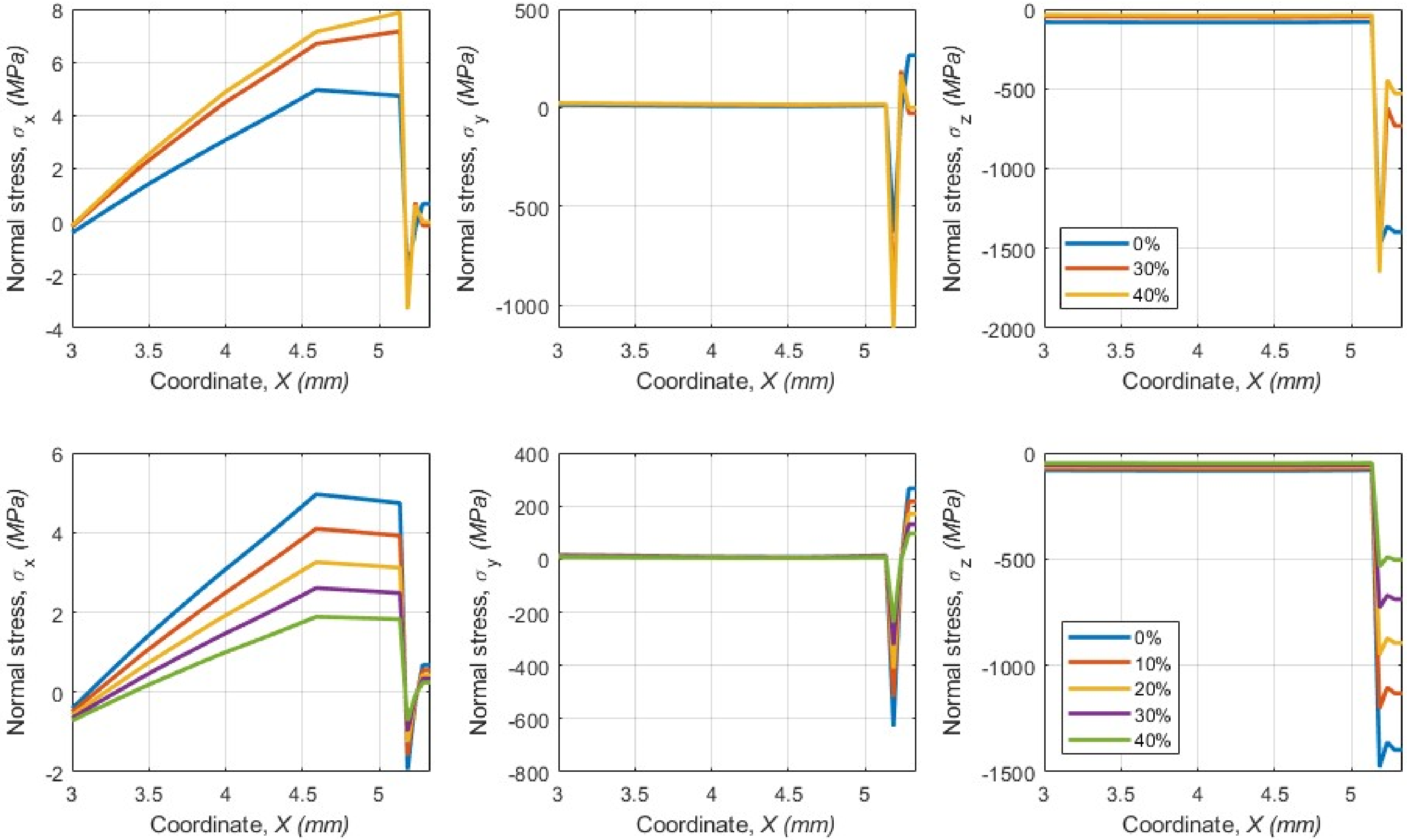

Design porosity in layers 1, 3, 5, 6

Same porosity in all six layers

Results

Effect of porosity

- Same porosity 40% in all layers
- Temperature 1000 ^{o}C

Max total deformation is reduced to 0.0896 mm from 0.1115 mm

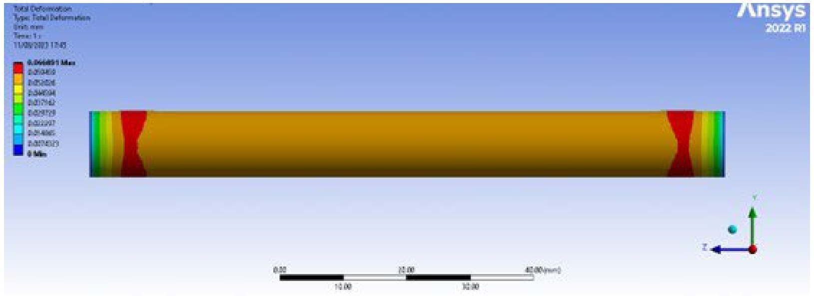

Layer 1

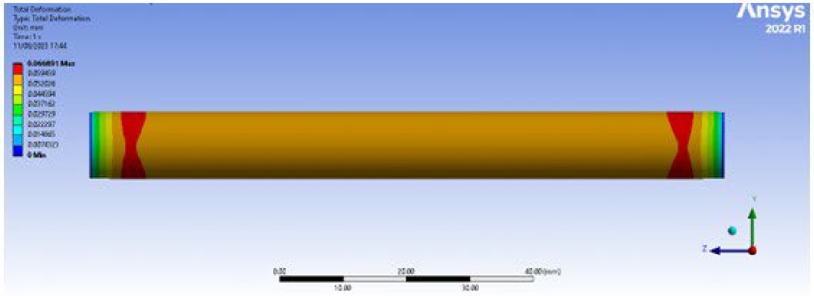

Layer 2

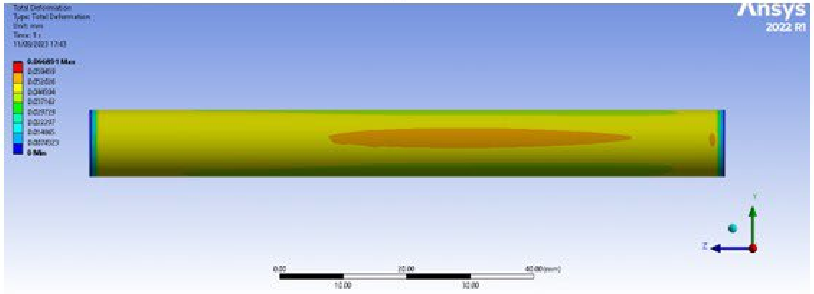

Layer 3

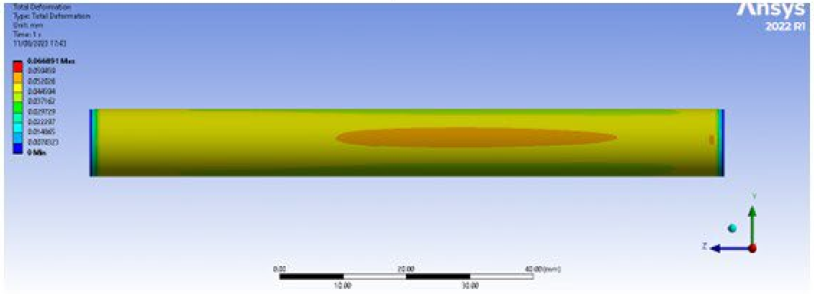

Layer 4

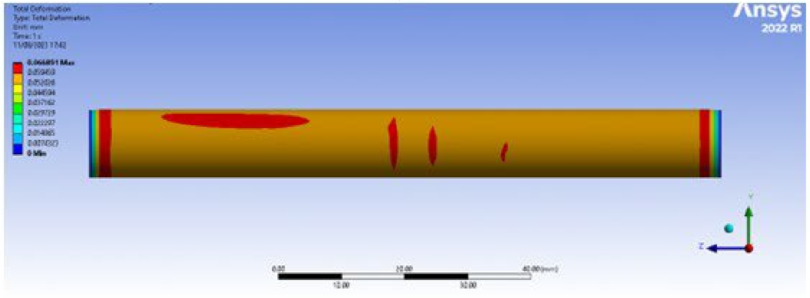

Layer 5

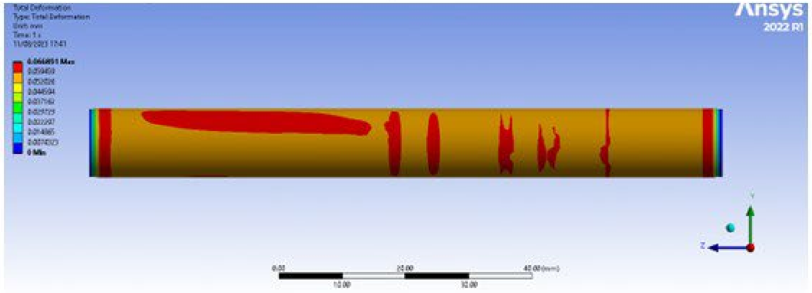

Layer 6

Summary

Conclusions:

- ☐ Identified areas of potential crack occurrence and delamination.
- ☐ Important impact of the difference in the CTE among the layers.
- ☐ Visible effects in the outer layer at 1000 °C due to melting of the silver.
- ☐ Total deformation increases about 1.4 times with the temperature growth from 600 to 800 °C for the non-porous structure.
- ☐ Increase in porosity from 30% to 40% may lead to approximately 10% reduction in the total deformation.

Next steps:

- ☐ Electrochemistry and fluid dynamics analysis, accounting for the thermomechanical deformation.
- ☐ Benchmarking with the high temperature SOEC tests in the laboratory.

Acknowledgements

The authors acknowledge high temperature steam electrolysis related funding by the UKRI EPSRC via Grant No. EP/W033178/1 (METASIS).

Thank you

Please, feel free to get in touch:

Professor Nadimul Faisal (RGU) n.h.faisal@rgu.ac.uk

Dr Victoria Kurushina (RGU) v.kurushina@rgu.ac.uk, v.kurushina@outlook.com

EP/W033178/1

Scalable metamaterial thermally sprayed catalyst coatings for nuclear reactor high temperature solid oxide steam electrolysis (METASIS)

Robert Gordon University Researchers
- Dr Victoria Kurushina, PDRF
- Vinooth Rajendran, RA

Investigators
- Prof Nadimul Faisal
- Prof Mamdud Hossain
- Dr Anil Prathuru

University of Surrey Researcher
- Dr Ajith Soman, PDRF

Investigators
- Dr Bahman Horri
- Dr Qiong Cai

ROBERT GORDON UNIVERSITY ABERDEEN

Engineering and Physical Sciences Research Council

UNIVERSITY OF SURREY